AGU PUBLICATIONS

JGR

Journal of Geophysical Research: Space Physics

RESEARCH ARTICLE
10.1002/2014JA020933

Key Points:
- Chemical and thermal impacts of sprites in the mesosphere are calculated
- The calculated concentration of electrons exhibits a significant enhancement
- The model predicts an increase in the gas temperature at low altitudes

Supporting Information:
- Text S1, Figures S1 and S2, and Tables S1–S30

Correspondence to:
F. C. Parra-Rojas,
fpr@iaa.es

Citation:
Parra-Rojas, F. C., A. Luque, and F. J. Gordillo-Vázquez (2015), Chemical and thermal impacts of sprite streamers in the Earth's mesosphere, *J. Geophys. Res. Space Physics*, *120*, 8899–8933, doi:10.1002/2014JA020933.

Received 10 DEC 2014
Accepted 4 JUN 2015
Accepted article online 8 JUN 2015
Published online 15 OCT 2015

Chemical and thermal impacts of sprite streamers in the Earth's mesosphere

F. C. Parra-Rojas[1], A. Luque[1], and F. J. Gordillo-Vázquez[1]

[1]Departamento del Sistema Solar, Instituto de Astrofísica de Andalucía, CSIC, Granada, Spain

Abstract A one-dimensional self-consistent model has been developed to study the chemical and thermal effects of a single sprite streamer in the Earth's mesosphere. We have used sprite streamer profiles with three different driving current durations (5 ms, 50 ms, and 100 ms) between 50 and 80 km of altitude and considering a kinetic scheme of air with more than 90 chemical species. Our model predicts strong increases in practically all the concentrations of the species studied at the moment of the streamer head passage. Moreover, their densities remain high during the streamer afterglow phase. The concentration of electrons can reach values of up to 10^8 cm^{-3} in the three cases analyzed. The model also predicts an important enhancement, of several orders of magnitude above ambient values, of nitrogen oxides and several metastables species. On the other hand, we found that the 4.26 μm IR emission brightness of CO_2 can reach 10 GR at low altitudes (< 65 km) for the cases of intermediate (50 ms) and long (100 ms) driving currents. These results suggest the possibility of detecting sprite IR emissions from space with the appropriate instrumentation. Finally, we found that the thermal impact of sprites in the Earth's mesosphere is proportional to the driving current duration. This produces variations of more than 40 K (in the extreme case of a 100 ms driving current) at low altitudes (< 55 km) and at about 10 s after the streamer head.

1. Introduction

Transient luminous events (TLEs) are large and short-lived (< 100 ms) optical flashes that occur between the lower stratosphere and ionosphere associated to thunderstorm activity in the troposphere as hypothesized by *Wilson* [1925]. The most common of these phenomena are the so-called sprites which were discovered serendipitously by *Franz et al.* [1990]. Sprites are huge weakly ionized plasma structures [*Neubert*, 2003; *Pasko*, 2003] whose extension goes from the lower ionosphere (80–85 km) through the mesosphere down to 40 km of altitude approximately. Sprites are produced by air electric breakdown caused by mesospheric electrons heated by the quasi-electrostatic (QE) fields induced by lightning discharges [*Pasko et al.*, 1995; *Cho and Rycroft*, 1998]. The QE field is mainly generated by positive cloud-to-ground (+CG) lightning strokes [*Boccippio et al.*, 1995] although it can also be produced by negative cloud-to-ground (−CG) lightnings with a great charge moment change [*Barrington-Leigh et al.*, 1999; *Taylor et al.*, 2008]. The runaway electron avalanche process can also be considered as a sprite initiation mechanism. Some previous studies have associated sprite emissions at low altitude with high energetic runaway electrons [*Bell et al.*, 1995]. *Füllekrug et al.* [2010], through low-frequency radio observations, detected electromagnetic pulses associated with an electron avalanche a few milliseconds after the causative lightning discharge coinciding with the sprite luminosity. These researchers concluded that relativistic runaway breakdown could emit broadband electromagnetic pulses and possibly generate sprites.

The first sprite images taken from a plane were published by *Sentman et al.* [1995]. These first sprite color pictures showed that reddish optical emission predominates at the top of sprites while bluish emissions are the most visible at the bottom of sprites. Since then, there have been many observations from ground [*Rairden and Mende*, 1995; *Lyons*, 1996; *Winckler et al.*, 1996; *Stanley et al.*, 1999; *Gerken et al.*, 2000; *Barrington-Leigh et al.*, 2001; *Stenbaek-Nielsen et al.*, 2013], from balloons [*Bering et al.*, 2004; *Bhusal et al.*, 2004], from the Space Shuttle [*Vaughan et al.*, 1992; *Boeck et al.*, 1995, 1998; *Yair et al.*, 2004], and from the International Space Station [*Blanc et al.*, 2004; *Jehl et al.*, 2013]. There are also observations from other space platforms such as FORMOSAT-2, using the instrument ISUAL (Imager of Sprites and Upper Atmospheric Lightnings) in operation since 2004. ISUAL has recorded photometric data in the visible and ultraviolet optical range [*Kuo et al.*, 2005; *Mende et al.*, 2005; *Liu et al.*, 2006; *Adachi et al.*, 2006, 2008; *Liu et al.*, 2009], as well as images [*Chen et al.*, 2008]. It is now

well established that sprites exhibit a common structure with three distinct regions [*Pasko et al.*, 1998; *Pasko and Stenbaek-Nielsen*, 2002]: an upper diffuse region (90–80 km), a middle transition region (80–75 km), and a lower region where streamers are visible (< 75 km). The values of the above mentioned altitudes are average and depend on, among other factors, the characteristics of the lightning precursor. Subsequent ground-based observations with better resolution [*Gerken et al.*, 2000; *Gerken and Inan*, 2003, 2005] and with high-speed cameras [*Marshall and Inan*, 2005, 2006; *Cummer et al.*, 2006; *McHarg et al.*, 2007; *Stenbaek-Nielsen et al.*, 2007] have shown a complex set of streamers in the lower part of sprites as well as various types of sprites [*Bór*, 2013]. In addition, high-speed sprite imaging has also shown a great similarity with streamer discharges at atmospheric pressure [*Raizer*, 1991; *Raizer et al.*, 1998]. Sprite streamers generally develop downward [*Moudry et al.*, 2003; *Cummer et al.*, 2006; *McHarg et al.*, 2007]. However, some upward streamer propagation has also been reported [*Cummer et al.*, 2006; *Stenbaek-Nielsen and McHarg*, 2008].

The first spectroscopic sprite observations [*Mende et al.*, 1995; *Hampton et al.*, 1996; *Morrill et al.*, 1998] with low spectral (between 10 nm and 6 nm) and temporal resolution (at standard video rate) identified the $1PN_2$ transition ($N_2(B^3\Pi_g) \rightarrow N_2(A^3\Sigma_u^+)$) as the most important optical emissions from sprites in the 550–840 nm spectral range. Subsequent modeling studies [*Pasko et al.*, 1997] confirmed that $1PN_2$ and $2PN_2$ ($N_2(C^3\Pi_u) \rightarrow N_2(B^3\Pi_g)$) were the molecular transitions responsible for the red and blue optical emission features apparent in sprite spectra as previously suggested by *Sentman et al.* [1995]. Later on, *Heavner* [2000] and *Heavner et al.* [2010] confirmed the presence of ultraviolet (UV) emission in sprite spectra. The blue optical emission has also been associated with $N_2^+(B^2\Sigma_u^+)$ [*Armstrong et al.*, 1998, 2000; *Morrill et al.*, 2002], although it is not usually detected in sprite spectra [*Armstrong et al.*, 2000]. Some studies have reported the possible presence of Meinel ($N_2^+(A^2\Pi_u) \rightarrow N_2^+(X^2\Sigma_g^+)$) emission in sprite spectra [*Morrill et al.*, 1998] that tend to be more apparent at lower layers of the atmosphere [*Bucsela et al.*, 2003]. On the other hand, the confirmation of the presence of $1NN_2$ ($N_2^+(B^2\Sigma_u^+) \rightarrow N_2^+(X^2\Sigma_g^+)$) in sprite spectra is important since it indicates that sprites can also excite electronic levels of ionized species.

Sprites (and other TLEs) can also emit in the IR and UV [*Liu et al.*, 2006] due to the excitation of species such as CO_2, N_2, NO, and/or N_2^+. However, the IR and UV emissions are mainly reabsorbed by H_2O and O_2 and O_3, respectively. Therefore, the detection of IR and UV features in sprite spectra needs to be done from space, from balloons or from high-altitude planes. There are some models of the near-ultraviolet and near-infrared (NIR) TLE optical emission and detection from space [*Picard et al.*, 1997; *Milikh et al.*, 1998; *Luque and Gordillo-Vázquez*, 2011; *Gordillo-Vázquez et al.*, 2011, 2012]. Other modeling work on NO-γ ($(NO(A^2\Sigma^+) \rightarrow NO(X^2\Pi_r))$ emissions in ultraviolet and Lyman-Birge-Hopfield (LBH, $N_2(a^1\Pi_g) \rightarrow N_2(X^1\Sigma_g^+)$) optical emission in the far-UV shows that, at 70 km, UV emissions from NO are less intense than those due to LBH emission from N_2 [*Liu and Pasko*, 2005, 2007]. The LBH emission has been detected by ISUAL [*Mende et al.*, 2004] and compared with streamer models [*Liu et al.*, 2006]. Contrarily, to LBH optical emissions, the emission of NO-γ from sprites has not yet been detected not even from space.

Regarding precise determination of the gas temperature in the TLE surrounding the atmosphere, it is worth mentioning that the recording of TLE spectra with the instrument Granada Sprite Spectrograph and Polarimeter between 700 nm and 800 nm and with a spectral resolution of 0.07 nm/pixel or 0.25 nm will allow to better resolve TLE spectra and to be able to quantify a possible local heating due to TLE activity in the lower mesosphere [*Passas et al.*, 2014; *Parra-Rojas et al.*, 2013b].

Although spectroscopic data provide valuable information about the excited species, the full impact of sprites in the chemical composition of the mesosphere is not well determined by spectroscopic means. Measurements by ISUAL between 40 and 60 km indicate that the mean energy of the electrons and the electric field underlying the optical spectra of sprites are, respectively, between 6.2–9.2 eV and 243–443 Td [*Kuo et al.*, 2005]. It is thus possible that these intense electric fields create highly reactive chemical species (such as energetic electrons, ions, and NO_x) that can induce local changes in the chemical [*Sentman and Wescott*, 1995; *Stenbaek-Nielsen et al.*, 2000] and electrical [*Gordillo-Vázquez and Luque*, 2010] properties of the mesosphere. The dipolar electric field and the electromagnetic pulse generated by CG lightning strokes also affect the electron concentration in the mesosphere and lower ionosphere [*Taranenko et al.*, 1993; *Shao et al.*, 2012]. Recent kinetic simulations of halos carried out by *Parra-Rojas et al.* [2013a] predicted an increase of up to 70 cm^{-3} in the mesospheric electron density due to the action of tropospheric +CG lightning. The enhanced electron concentration can stay high between 10 and 100 s after the current peak of the parent positive lightning discharge. In this regard, *Luque and Gordillo-Vázquez* [2012] showed that the electron production due to

associative detachment (AD) of O^- by N_2 could be responsible for the delayed sprites [*Bell et al.*, 1998; *Cummer and Füllekrug*, 2001] that occur more than 10 ms after the parent lightning stroke.

A present line of active research is focussed in understanding how sprites and their postdischarge phase affect the atmospheric chemistry of NO_x and N_2O. Variations of NO and O_3 concentrations due to blue jets exhibit enhancements between, respectively, 10% and 0.5% at 30 km altitude [*Mishin*, 1997]. However, according to *Parra-Rojas et al.* [2013a], the concentrations of NO and O_3 exhibit a negligible variation due to halos. Moreover, the simulations by *Hiraki et al.* [2004] predict a substantial increase in the concentration of $O(^1D)$, and the measurements made by UARS (Upper Atmosphere Research Satellite) indicate a substantial enhancement of $O(^1S)$ [*Lee and Shepherd*, 2010] due to the possible presence of sprites. Concerning kinetic modeling of sprites, *Sentman et al.* [2008] developed a kinetic model with more than 800 chemical reactions to study the impact of a streamer pulse with $E_{max} = 5E_k$ (where E_k is the breakdown electric field, $E_k/N = 120$ Td) and $\Delta t = 6$ μs at 70 km of altitude in the mesosphere. With this model, *Sentman et al.* [2008] estimated an increase of the streamer head electron density of up to 10^6 cm^{-3} persisting about 1 s. These authors also estimated an increase in the concentration of NO by 50%, while *Hiraki et al.* [2008] estimated an increase of 4 orders of magnitude in the density of NO at the same altitude. *Enell et al.* [2008], however, predicted an increase of 50% in the concentration of NO_x at 73 km. *Gordillo-Vázquez* [2008, 2010], employing a reduced electric field of 400 Td, found increases of an order of magnitude in the concentration of NO and NO_2 while for the density of NO_3 predicted an increase of more than 3 orders of magnitude at 68 km. Moreover, *Gordillo-Vázquez* [2008] was also able to calculate the brightness of the sprite-related CO_2 4.3 μm IR emission predicting a value as high as 100 MR at 68 km of altitude that pointed to its possible detection from space. The substantial differences found between the different sprite kinetic model predictions may be due to different initial conditions employed and to the use of different rates for different numbers of processes. The results by *Arnone et al.* [2008], through analysis of the data recorded by Michelson Interferometer for Passive Atmospheric Sounding aboard Envisat (Environmental Satellite), showed a possible sprite-induced NO_2 enhancement of about 10% at 52 km of altitude in correspondence with active thunderstorm and with a tendency to grow up with height. Also aboard Envisat but using the Global Ozone Monitoring by Occultation of Stars instrument, *Rodger et al.* [2008] showed that there is no significant global impact of sprites and other TLEs in the concentration of NO_x at altitudes between 20 and 70 km. The possible chemical impact of the sprite streamer tails in the mesosphere was also investigated by *Sentman and Stenbaek-Nielsen* [2009] at 70 km of altitude. In this case, assuming undervoltage conditions ($E = 0.5E_k$), the electron concentration decreases smoothly due to dissociative attachment of electrons to molecular oxygen O_2. More recently, *Evtushenko et al.* [2013] developed a self-consistent model to study the influence of sprites on the mesosphere as a function of the altitude. They obtained the maximum of the electron density variation at 75 km together with an important increase in the concentration of the metastable $N_2(A^3\Pi_u^+)$ between 72 and 76 km.

As reported by *Stanley et al.* [2000], sprites can also occur during daytime triggered by exceptionally large lightnings. Later on, *Farges et al.* [2005] and *Kumar et al.* [2008] also detected daytime sprites through infrasound and VLF perturbations, respectively. The chemical fingerprint of daytime sprites on the mesosphere is not well known presently. In this regard, the simulations by *Winkler and Nothold* [2014] suggest a depletion in the ozone concentration (~15%) under the action of diurnal sprites.

In the present work, we aim to contribute to the fundamental understanding of the chemistry of nonequilibrium plasmas produced by nighttime sprite streamers in the mesosphere and their influence on the mesosphere chemical composition and thermal evolution. This paper describes the kinetic model used, the time evolution of the concentration of many important species for the sprite, and its afterglow through an upgrade of the self-consistent model by *Parra-Rojas et al.* [2013a]. We study the processes involved in the chemistry of the atmosphere under the action of sprite streamers with three different driving currents between 50 km and 80 km. Although the model is less reliable as we descend in altitude because, below 70 km, sprite streamers often branch, we think that the model is quite realistic between 80 and 70 km. It is nevertheless interesting to show the approximate chemical and thermal evolution of the atmosphere at lower (< 70 km) altitudes under the action of sprite streamers. We also discuss in the paper the main instantaneous optical emission of sprites in the visible ($1PN_2$ and $2PN_2$) and infrared (4.26 μm and 14.9 μm) together with the optical emissions as seen by cameras recording at 33 fps and 1000 fps. Finally, we present a detailed study of the local thermal impact of sprite streamers in the Earth's mesosphere describing the most important mechanisms responsible for the local energy exchange between sprite streamers and the surrounding atmosphere.

The structure of this paper consists, first, of a description of the model and its basic equations together with the processes taken into account (section 2). Then, in section 3, we describe and discuss the main results. Finally, the conclusions are presented in section 4. Furthermore, in the supporting information we list all the chemical processes used in the model and their reaction rates. We also provide the statistical weights of CO_2 together with all the potential energies (and how they were obtained) of the chemical species that are needed to perform the energy balance.

2. Model

Although sprites have a downward development, this kinetic model does not aim to study the vertical evolution of sprite streamers but to understand how a single sprite streamer can chemically and thermally affect each layer of the mesosphere. It is known that a single streamer tends to branch as it propagates downward. For the sake of simplicity we are neglecting here this branching dynamics and, consequently, our model can only be considered as a pseudo 1-D model.

The kinetic model used here is an upgrade of the one by *Parra-Rojas et al.* [2013a] with 97 chemical species and more than 900 kinetic processes. It integrates a set of differential equations to model the chemical and thermal behaviors of the air plasma generated by sprite streamers. The temporal evolution of the density of each species i is obtained through

$$\frac{\partial n_i}{\partial t} = G_i - L_i, \tag{1}$$

where n_i is the concentration of each chemical species (molecular and atomic neutrals, positive and negative ions, free electrons, etc.) and G_i and L_i are the rates of, respectively, the gain and loss processes during the simulation. The electron energy distribution function (EEDF) is also obtained to calculate the reaction rates of the electron impact processes. To do this, equation (1) is solved self-consistently with the steady state Boltzmann transport equation

$$\frac{e\mathbf{E}(t)}{m_e} \cdot \nabla_{\mathbf{v}} f(\mathbf{v}, t) = \left(\frac{\partial f}{\partial t}\right)_{\text{collisions}}, \tag{2}$$

where $f(\mathbf{v}, t)$ is the velocity distribution function of free electrons at time t and velocity $\mathbf{v}$ and e, m_e, $\mathbf{E}(t)$, and $\nabla_{\mathbf{v}}$ represent the elementary charge, the mass of the electron, the local electric field, and the velocity gradient operator, respectively. The effects of collisions between electrons and heavy particles have been included in the right-hand side of equation (2). Coulomb interactions between electrons are negligible due to their low density in the upper atmosphere.

Finally, we studied the thermal influence of sprite streamers in the surrounding atmosphere by considering the balance between the processes that inject energy into the gas and the mechanisms which extract energy from it. The processes that contribute to increase the gas temperature are partial reabsortion of radiated energy by the surrounding atmosphere and the absorption of energy from an external power source. The corresponding powers of each of these two mechanisms are P_{abs} and P_{ext} for the reabsortion and for the absortion of an external energy, respectively. The reabsorption power is expressed by

$$P_{\text{abs}} = k_{\text{corr}} \sum_j n_j \frac{A_{ij} h\nu_{ji}}{4\pi N} \frac{g_i}{g_j} \frac{1}{\exp\left(\frac{h\nu_{ji}}{k_b T_{\text{gas}}^{\text{bg}}}\right) - 1}, \tag{3}$$

where k_{corr} is a correction factor of the gas temperature (we will explain it below), n_j is the population of the lower absorbing level in each transition considered, A_{ij} is the Einstein spontaneous emission probability, $h\nu_{ji}$ is the energy needed to excite a molecule from a lower level j to an upper level i, N is the total gas number density, g_i and g_j are the statistical weights of the upper and lower excited levels, respectively, k_B is the Boltzmann constant, and $T_{\text{gas}}^{\text{bg}}$ is the background gas temperature. The process represented by P_{abs} is the radiative power partially reabsorbed by the air plasma from the surrounding atmosphere at a constant temperature $T_{\text{gas}}^{\text{bg}}$. The power directly deposited into the gas by the streamer electric field is what we have called external power, P_{ext}, given by

$$P_{\text{ext}} = e n_e v_e \frac{E}{N}, \tag{4}$$

where e is the elementary charge, n_e and v_e are the electron density and drift velocity, respectively, and E/N is the reduced electric field. The powers deposited into the gas (P_{abs} and P_{ext}) are redistributed through different channels. The term P_{elec} is the power that goes to the translational degrees of freedom of electrons in the plasma, and it is obtained through

$$P_{elec} = \frac{3}{2}\frac{k_B}{N}\frac{d(n_e T_e)}{dt}, \tag{5}$$

where T_e is the electron temperature. A large percentage of the deposited power goes to the translational degree of freedom of the gas, P_{gas}, represented by

$$P_{gas} = \frac{\gamma}{\gamma - 1} k_B \frac{dT_{gas}}{dt}, \tag{6}$$

where γ is the specific gas heat ratio of dry air ($\gamma = 1.4$) and T_{gas} is the gas temperature. Another important channel in which the powers P_{abs} and P_{ext} are redistributed into the internal degrees of freedom of the gas is the chemical power, P_{chem}, given by

$$P_{chem} = \frac{1}{N}\sum_i Q_i \frac{dn_i}{dt}, \tag{7}$$

where Q_i is the potential energy or the standard enthalpy of formation of species i. Note that P_{chem} can be positive or negative depending on the sign of Q_i or dn_i/dt. In the case of negative chemical power, this released power can go to the gas heating. Finally, the power released during spontaneous radiative emission, P_{rad}, reads as

$$P_{rad} = \frac{\kappa^*}{N}\sum_i h\nu_{ij} A_{ij} n_i, \tag{8}$$

where $h\nu_{ij}$ is the energy released during radiative decay from an upper level i to a lower level j. The assumed factor κ^* (equal to 0.5) accounts for the reabsortion coefficient calculated through the mean free path of the CO_2 IR photons [*López-Puertas*, 1982] in a sprite streamer of 50 m of average diameter. All these terms are included in the power balance equation

$$P_{abs} + P_{ext} = P_{elec} + P_{gas} + P_{chem} + P_{rad}. \tag{9}$$

The zero-dimensional simulations were performed for a pressure range equivalent to altitudes between 50 km and 80 km using ZDPlasKin, a tool developed by *Pancheshnyi et al.* [2008] that incorporates the BOLSIG+ solver to calculate the EEDF [*Hagelaar and Pitchford*, 2005].

The simulation process basically consists of three stages. The first step is what we have called electronic relaxation of our kinetic scheme which translates into the relaxation of our system of kinetic equations. In this stage (based in the relaxation stage of *Sentman et al.* [2008] and *Parra-Rojas et al.* [2013a]) we use a reduced electric field $E/N \sim 0$ Td during a simulation time $t \sim 10^6$ s. With this preliminary simulation we obtain a chemical equilibrium consistent with the background electron density estimated by *Hu et al.* [2007]. In doing this, we calculated the equilibrium concentrations of the ionized and excited species considered together with consistent rates of ionization and dissociative ionization of N_2, O_2 due to the flux of galactic cosmic rays [*Yelinov et al.*, 2009]. The initial ambient densities of the neutral species used at each altitude were taken from the Whole Atmosphere Community Climate Model [*Marsh et al.*, 2013].

The second step is the thermal relaxation of our system of equations, and it is very similar to the previous stage. Using the concentrations obtained through the previous electronic relaxation stage, we get, for each altitude, a parameter (k_{corr} in P_{abs}) to keep constant the gas temperature at long times ($t \sim 3 \times 10^4$). In the nighttime atmosphere (without solar photochemistry) with no external perturbations ($E = 0$), the gas temperature tends to decrease by emitting thermal radiation (cooling). The introduction of the k_{corr} factor (added ad hoc) in the expression of P_{abs} contributes to partially compensate this effect and allows us to obtain a more accurate thermal impact of sprites on the surrounding atmosphere.

Finally, the third stage is the main simulation in which we calculate the thermal and chemical impact of sprites in the mesosphere. For this we need to estimate first the local electric field as a function of time at each of

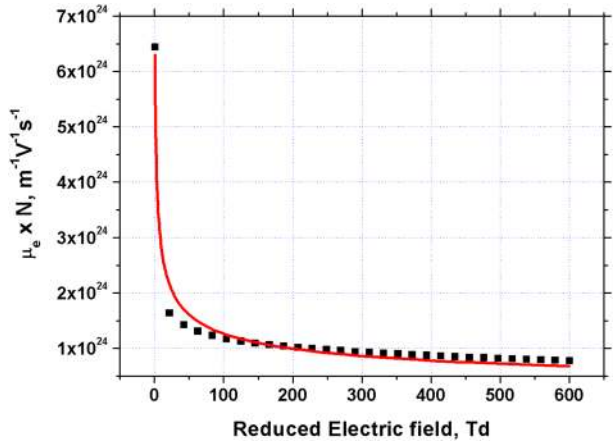

Figure 1. Dependence of $\mu_e N$, where μ_e is the electron mobility and N is the gas density, upon the reduced electric field in dry air. The solid red line is the power fit with a correlation coefficient of 0.9808.

the altitudes of interest. However, externally imposing this electric field as derived from independent microscopic simulations leads to unrealistic predictions since small differences in the rates of ionization between two models grow exponentially and often result in wildly overestimated electron densities. Following *da Silva and Pasko* [2014], we have found it more convenient to impose an electric current as input, instead of the electric field. As we will see now, this provides a certain degree of self-consistency in the sense that an overshoot in the electron density is quickly damped by the consequent decrease in the electric field.

We have calculated the electric field associated with a sprite streamer through the microscopic Ohm law

$$J = \sigma E, \tag{10}$$

where J is the current density, σ is the electron conductivity, and E is the electric field. The electron conductivity has a strong dependence with the electron density and mobility that in turn depends on the electric field as

$$\sigma = en_e\mu_e(E/N), \tag{11}$$

where μ_e is the electron mobility. We used BOLSIG+ to obtain the dependence of $\mu_e N$ on the reduced electric field in an air plasma with exactly the same composition as ours. Once calculated, we fitted $\mu_e N$ to a power law (see Figure 1).

$$\mu_e N = a\left(\frac{E/N}{1Td}\right)^b, \tag{12}$$

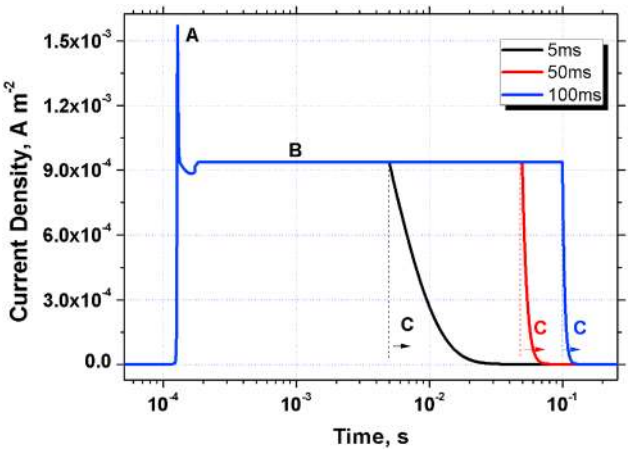

Figure 2. Time evolution of the current density of a sprite streamer at 75 km of altitude. The black, red, and blue lines are for driving currents of 5 ms, 50 ms, and 100 ms, respectively. Label A corresponds to the streamer head, B corresponds to the driving current, and C (black, red, and blue) is associated to the postafterglow stages.

where we found $a = 6.3 \times 10^{24}$ m^{-1} V^{-1} s^{-1} and $b = -0.35$. Using equations (10) and (11), we derived and approximate expression for the reduced electric field in a sprite streamer channel as

$$\frac{E}{N} = \left(\frac{J}{en_e a}\right)^{\frac{1}{b+1}} \times 1Td. \tag{13}$$

In our simulations, the externally imposed current consists of three phases (see Figure 2): (a) a peak corresponding to the passage of the streamer head, (b) a constant plateau, and (c) an exponential decay with a time constant of 4 ms. For the streamer head (a) we run microscopic streamer simulations similar to those described by *Luque et al.* [2008] and *Luque and Ebert* [2010]. For each altitude h we run a streamer simulation with the

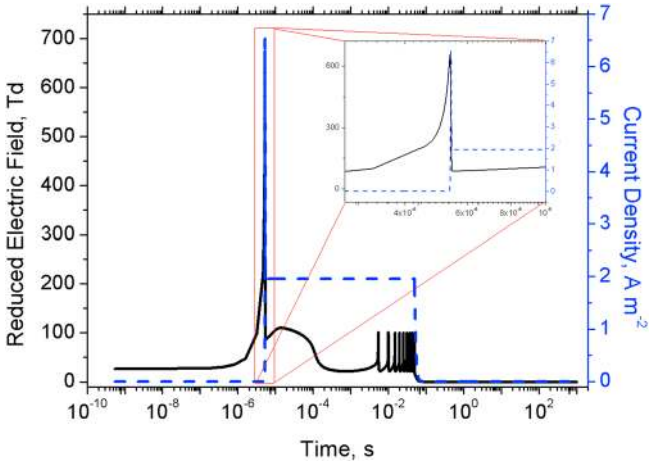

Figure 3. Reduced electric field (black solid line) and current density (blue dotted line) temporal behavior of a single sprite streamer at 50 km of altitude with a driving current duration of 50 ms.

background electron density resulting from the kinetic electronic relaxation stage and a Gaussian ionization seed a few kilometers above*h* that was later on used as an input in the kinetic model. We then recorded the resulting electric current at *h*. In Figure 14 of the work by *Stenbaek-Nielsen et al.* [2013], we can see an image of a single sprite streamer whose width, at 76 km of altitude, could be approximately 500 m. According to *Pancheshnyi et al.* [2005], the streamer electrodynamic radius can be a factor 2 greater than the optical radius. We have rescaled the streamer diameter with the inverse of the density (for each altitude) establishing a reference sprite streamer diameter of 1 km at 76 km. With this sprite streamer rescaling of its radius, the current flowing through the streamer channel is ≃190 A and ≃1120 A at 80 km and 50 km, respectively. In this way, our current density becomes consistent with the sprite core currents estimated by *da Silva and Pasko* [2014].

The currents resulting from these simulations contain first a strong peak due to the field enhancement at the streamer head and then a reenhancement of the field that as argued by *Liu* [2010] and *Luque and Ebert* [2010] corresponds to the streamer afterglow. Microscopic simulations are limited to only a few milliseconds, but *Stenbaek-Nielsen and McHarg* [2008] report observations of sprite afterglows lasting up to 100 ms. It is to simulate these long-lasting afterglows that we extended the current input with a constant plateau (b) as mentioned above. We have used current durations of 5 ms, 50 ms, and 100 ms, as we can see in Figure 2. They are all terminated by an exponential decay (c) lasting 4 ms. To summarize, our model solves self-consistently equations (1), (2), (9), and (13) at each altitude of the mesosphere (between 50 km and 80 km) considering a complete set of chemical species under the action of a sprite streamer.

3. Results and Discussion

In this section, we show and discuss the effects of sprite streamers in the electric, chemical, and thermal properties of the mesosphere. Therefore, we have performed simulations with different driving current durations (after the streamer head) since we can have relatively high electric fields during a long time.

3.1. Reduced Electric Field

We start our analysis with the reduced electric field, which drives many of the chemical processes in our model. Figure 3 shows the evolution of the field at 50 km when the driving current lasts 50 ms. There the evolution is characterized by three features: (1) a strong peak, reaching 700 Td, produced by the passage of the streamer head and approximately coinciding with the peak of the driving current; (2) a reenhancement of the field to values close to the breakdown field 120 Td that lasts about 0.1 ms; and (3) a train of periodic oscillations starting around 6 ms and that persists up to the end of the driving current. With the exception of feature (3), which appears only at low altitudes (< 60 km), the overall behavior of the reduced field is similar at all altitudes. This is shown in Figures 4a–4f. All six figures extend the plots of reduced electric field and driving current to the complete range of altitudes considered in our model and to the three durations of the driving current used: 5 ms (a–d), 50 ms (b–e), and 100 ms (c–f).

In Figure 5 we plot the dependence with altitude of the maximum values of the reduced electric field and of the streamer current density, corresponding to the streamer head. Since the reduced field E/N is driven by the imposed current density J, the highest value of the reduced electric field and the highest value of the streamer current density are approximately simultaneous for any given altitude. Both peak values decrease with increasing altitude, so the absolute maxima are at the lowest considered altitude, 50 km (650 Td with 6.53 A m^{-2}).

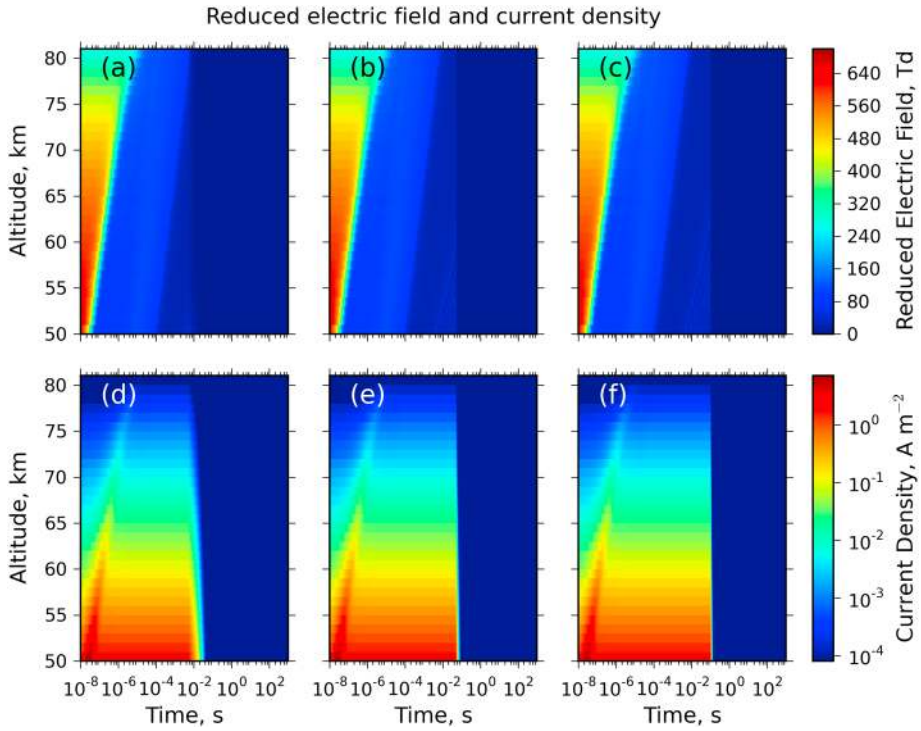

Figure 4. Altitude-time evolution of the (a–c) reduced electric field and (d–f) current density due to a single sprite streamer with a driving current of 5 ms (Figures 4a–4d), 50 ms (Figures 4b–4e), and 100 ms (Figures 4c–4f).

The second phase of the electric field evolution is the reenhancement to values close to the breakdown threshold. As we will see later, this reenhancement will play a relevant role in activating many chemistry pathways; we will refer to it as the *high-field phase* of the simulation. Figures 4a–4c show that the duration of this high-field phase depends on the altitude, scaling as $1/N$, and ranges from 10^{-4} s at 50 km to 10^{-2} s at 80 km of altitude. As we mentioned above, the third stage of the evolution of the electric field consists in a set of periodic oscillations and, as we appreciate in Figures 4b and 4c, they are only present below 60 km and when the driving current lasts 50 or 100 ms. This is a consequence of typical times scaling as $1/N$ combined with a duration of the driving current that does not depend on altitude.

The high-field phase and the oscillations appear during the driving current. Therefore, as shown in equations (10) and (11), the evolution of the electric field is partly determined by the electron concentration (the reduced electric field is inversely proportional to the electron density n_e and directly proportional to the current density). The high-field phase is produced by a small decrease in the electron concentration, just after the streamer head, caused by dissociative attachment of O_2

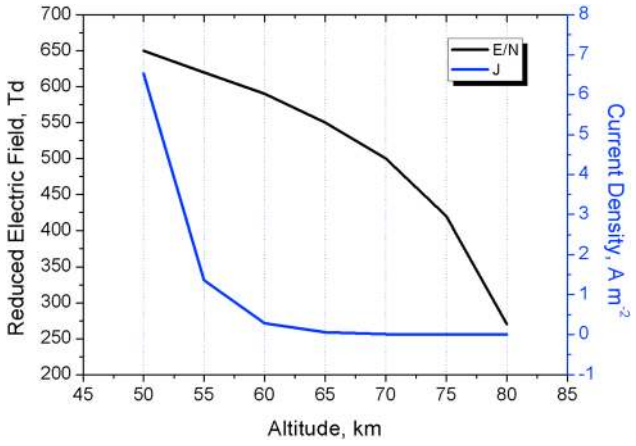

Figure 5. Altitude evolution of the maximum reduced electric field (black line) and maximum streamer current density (blue line).

$$P35: e + O_2 \rightarrow O^- + O.$$

This process pushes upward the electric field until it is high enough to cause significant electron impact ionization of O_2 and N_2:

$$P33: e + O_2 \rightarrow O_2^+ + e + e,$$

$$P22: e + N_2 \rightarrow N_2^+ + e + e$$

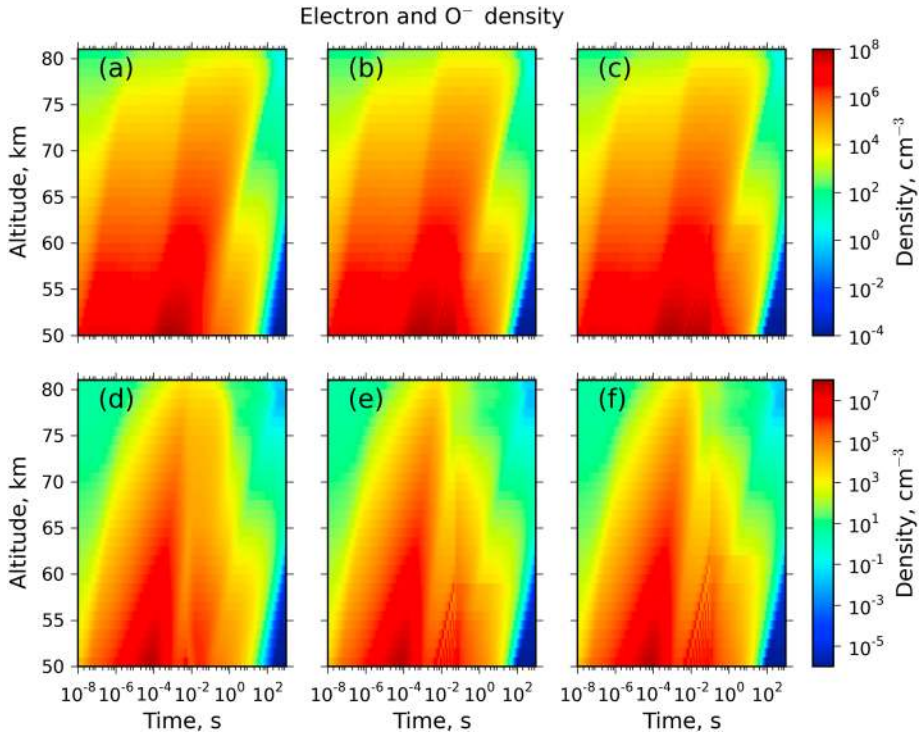

Figure 6. Altitude-time evolution of the (a–c) electron density and (d–f) O^- density due to a single sprite streamer with a driving current of 5 ms (Figures 6a–6d), 50 ms (Figures 6b–6e), and 100 ms (Figures 6c–6f).

and associative detachment of O^- by N_2:

$$P346 : O^- + N_2 \rightarrow N_2O + e.$$

The strong ionization produced by the streamer head (see times between 10^{-6} s and 10^{-4} s in Figures 6a–6c) screens the electric field so that after 10^{-4} s (at 50 km) and 10^{-2} s (at 80 km), it drops to around 20 Td. Consequently, the reaction constant of associative detachment (that depends on E/N) decreases to 2×10^{-13} cm^3 s^{-1} (see supplementary documentation of *Luque and Gordillo-Vázquez* [2012]), and electrons are removed by

$$P107 : e + O_4^+ \rightarrow O_2 + O + O.$$

With this decrease of the electron density (due to electron recombination with O_4^+) the reduced electric field increases strongly again during the constant driving current stage (see Figure 3) and activates the production of O^- (see Figure 6) through dissociative attachment of O_2. The strong periodic decrease of the reduced electric field from the pulse peak is due to the contribution of the three processes explained previously (P33, P22, and P346). Finally, when the driving current drops to zero, the reduced electric field vanishes.

We note that the oscillations in the electric field are, to some degree, a consequence of the imposition in our model of a constant electric current. They would probably disappear or be modified in models with a fully self-consistent calculation of the electric field. However, they may also indicate a physical tendency of the electric field to rise due to the removal of electrons at time scales of some tens of milliseconds. This higher electric field would be seen as a rebrightening of the lower portions of decayed sprite tendrils. In Figure 7 we show the electric field at the lowest altitudes of our simulations; there we see that the oscillations appear as upward moving spots of increased luminosity. We speculate that these spots may be related with the so-called *crawlers*, described by *Moudry* [2003] as bright segments that move upward with a velocity of $10^4 - 10^5$ m/s. As seen in Figure 7, we obtain a velocity of about 10^5 m/s at 60 km.

3.2. Chemical Impact

In this section we discuss the evolution of atmosphere's chemical composition under the action of sprite streamers. We will illustrate it with two different kinds of figures: figures with six panels represent the evolution of two directly related chemical species, while figures with three panels represent a species. In both cases,

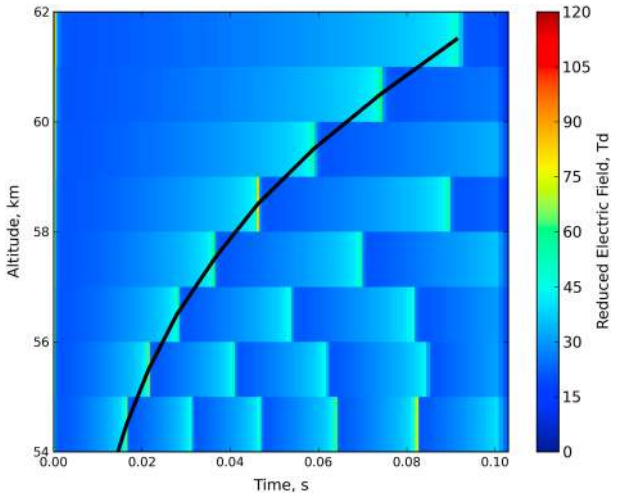

Figure 7. Altitude-time evolution of the reduced electric field oscillations during the driving current (50 ms duration) and between 54 and 62 km of altitude. The black line shows the upward movement of the possible crawlers [*Moudry*, 2003].

the first, second, and third columns are associated to a sprite streamer with driving current durations of 5 ms, 50 ms, and 100 ms, respectively.

3.2.1. Electron Density and O^-

We see in Figures 6a–6c the altitude and time dependence of the electron density for the three driving current durations that we considered. In the three cases, above 65 km, the electron concentration increases between 4 and 5 orders of magnitude in the streamer head due to N_2 and O_2 electron impact ionization:

$$P22 : e + N_2 \rightarrow N_2^+ + e + e,$$

$$P33 : e + O_2 \rightarrow O_2^+ + e + e,$$

electron impact ionization is the main mechanism producing electrons above breakdown ($E/N > 120$ Td) scenarios. When the reduced electric field falls down to subbreakdown values (after the streamer head), the electron concentration grows again by a factor 6 due to the associative detachment (AD) of O^- by N_2:

$$P346 : O^- + N_2 \rightarrow N_2O + e.$$

The electron density remains high for a few seconds due to AD, and it decreases later to background values due to the recombination processes

$$P107 : e + O_4^+ \rightarrow O_2 + O + O,$$

and

$$P108 : e + O_4^+ \rightarrow O_2 + O_2.$$

Below 65 km and at the time of passage of the streamer head, the electron density increases between 8 and 11 orders of magnitude due to ionization of N_2 and O_2. Between 10^{-4} s and 10^{-3} s after the passage of the streamer head, an increase of a factor of 6 occurs due to associative detachment (AD) of O^- by N_2. In the cases of 50 ms and 100 ms driving current durations (Figures 6b and 6c), and following the oscillations of the reduced electric fields, electron concentration changes due to the mechanisms P22, P33, P35, P107, and P346 commented in the previous section. After the electric field oscillations, the electron concentration remains elevated, around 10^5 cm^{-3}, up to nearly 100 s. Finally, the electron density returns to ambient values due to three-body electron attachment:

$$P39 : e + O_2 + O_2 \rightarrow O_2^- + O_2.$$

The concentration of the O^- anion is closely related to the temporal evolution of the electron density. The largest increase in the concentration of O^- is produced by the streamer head field, increasing between 14 and 5 orders of magnitude above its ambient value at, respectively, 50 km and 80 km of altitude (see Figures 6d–6f). The main chemical mechanism responsible for this strong increase is dissociative attachment (DA) of O_2

$$P35 : e + O_2 \rightarrow O^- + O.$$

When the reduced electric field goes below ~60 Td, the O^- density decreases by associative detachment of O^- by N_2, producing N_2O. This drop in the O^- ion concentration is directly related with the increase of the electron density through associative detachment. In the final stage of the simulation, when the electric field has dropped to zero, the O^- density returns to its ambient value due to AD with CO and O_2:

$$P359 : O^- + CO \rightarrow CO_2 + e,$$

and

$$P347 : O^- + O_2 \rightarrow O_3 + e.$$

For current durations of 50 ms and 100 ms, we observe in Figures 6e and 6f that the density of O^- decreases faster than in the case of 5 ms duration (see Figure 6d). This is due to the stronger influence of AD of O^- in those cases (50 ms and 10 ms). In these cases, and at middle altitudes (60–70 km), we see a small increase of O^- during the final stage of negligible reduced electric field due to charge transfer:

$$P362 : O_2^- + O \rightarrow O^- + O_2,$$

The O^- density returns smoothly to background values by associative detachment (AD) processes

$$P347 : O^- + O_2 \rightarrow O_3 + e,$$

$$P351 : O^- + O_3 \rightarrow O_2 + O_2 + e,$$

and charge transfer

$$P356 : O^- + O_3 \rightarrow O_3^- + O.$$

At low altitudes (below 60 km) we obtain variations in the concentration of O^- associated with the oscillations of the reduced electric field that we described above. The density of O^- remains at values between $10^3 - 10^5$ cm^{-3} up to 100 s after the passage of the streamer head.

3.2.2. N(^{2}D) and NO

Figures 8a–8c represent the density of excited atomic nitrogen N(^{2}D). The evolution of these species is closely related with the reduced electric field. Consequently, when the reduced electric field reaches a maximum, the N(^{2}D) density reaches values of up to 10^7 cm^{-3} and 10^5 cm^{-3} at, respectively, 50 km and 80 km of altitude. The main production process of N(^{2}D) is direct electron impact N_2 dissociative excitation:

$$P25 : e + N_2 \rightarrow N(^2D) + N + e.$$

These maximum values of the N(^{2}D) density persist during the high-field phase due to the balance between the electron impact dissociative excitation of N_2 (P25) and quenching by O_2:

$$P169 : N(^2D) + O_2 \rightarrow NO + O(^1D).$$

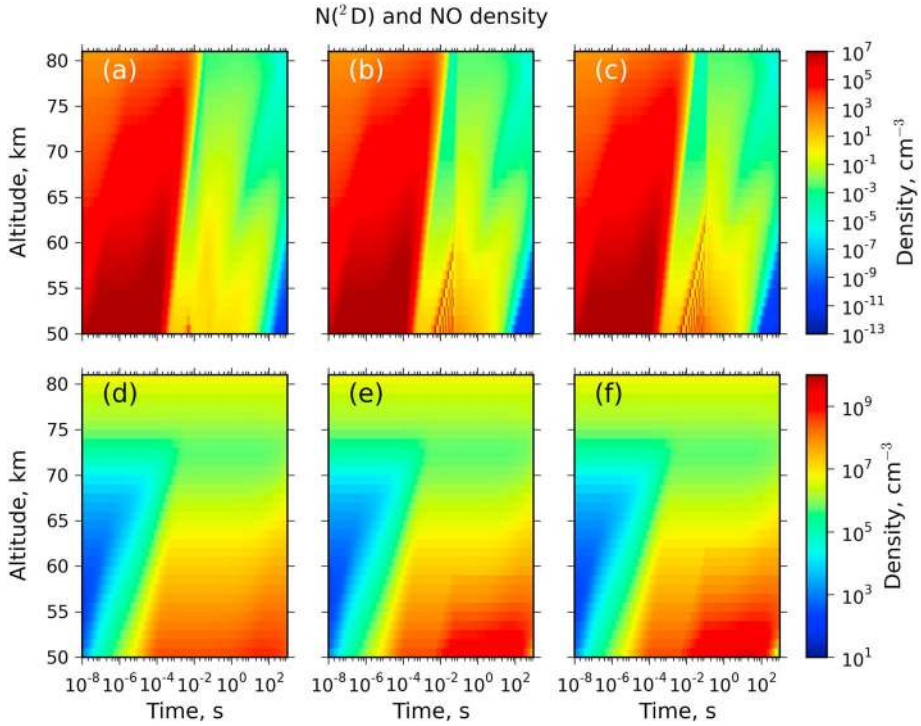

Figure 8. Altitude-time evolution of the (a–c) N(^{2}D) density and (d–f) NO density due to a single sprite streamer with a driving current of 5 ms (Figures 8a–8d), 50 ms (Figures 8b–8e), and 100 ms (Figures 8c–8f).

At the end of the high-field phase, the concentration of N(^{2}D) decreases slightly since P25 is less effective than quenching by O_2. When the reduced electric field vanishes, the density of N(^{2}D) still increases up to 2 orders of magnitude due to dissociative recombination of electrons with NO^+:

$$P101 : e + NO^+ \rightarrow N(^2D) + O,$$

once this process (P101) stops, the density of N(^{2}D) slowly returns to its background value due to quenching by O_2 (P169) at longer times. Between 65 and 50 km and in the cases of 50 ms and 100 ms of current durations (see Figures 8b and 8c, respectively), the density of N(^{2}D) grows more than 7 orders of magnitude above its background values due to the action of the reduced electric field oscillations.

The altitude and time dependence of the ground state NO density are shown in Figures 8d–8f. Note that, above 74 km, the impact of a sprite streamer in the NO concentration is negligible. Below this altitude the density of NO increases up to 8 orders of magnitude during the passage of the streamer head. The main mechanisms responsible for this strong variation are

$$P169 : N(^2D) + O_2 \rightarrow NO + O(^1D)$$

and

$$P168 : N(^2D) + O_2 \rightarrow NO + O.$$

When the driving current lasts 5 ms the density of NO remains unchanged during the complete simulation due to the balance between the gain and loss reactions

$$P413 : O + NO_2 \rightarrow NO + O_2,$$

$$P333 : O_2^+ + NO \rightarrow NO^+ + O_2.$$

In the rest of the considered cases, we see a secondary increase of up to 10^9 cm^{-3} in the concentration of NO. The oscillations of the reduced electric field underlie this strong NO enhancement since they induce the production of N(^{2}D) which generates NO after quenching (P168 and P169).

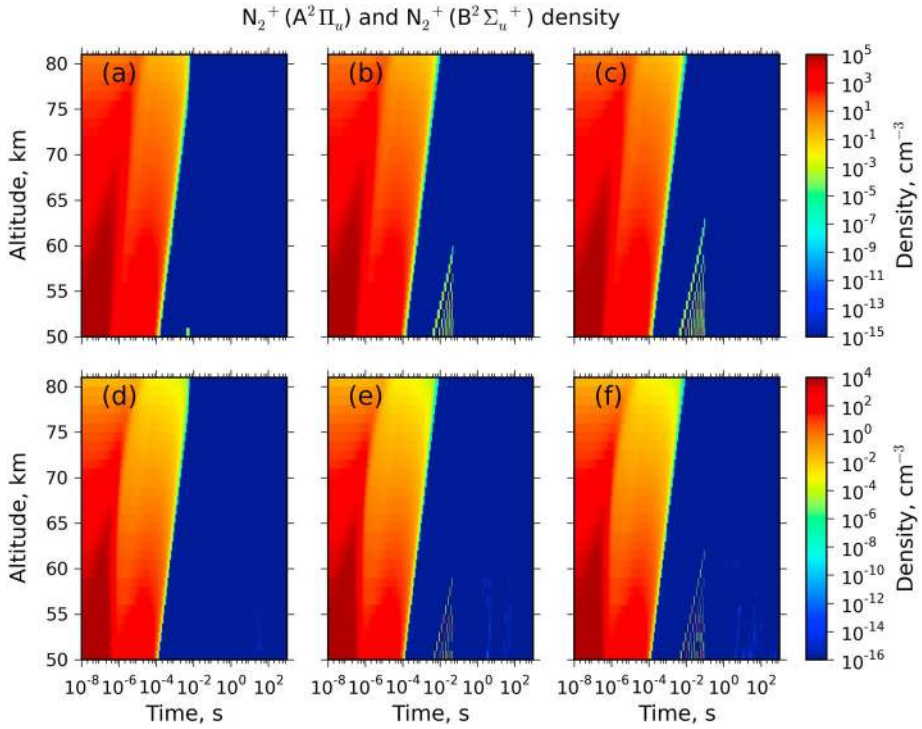

Figure 9. Altitude-time evolution of the (a–c) $N_2^+(A^2\Pi_u)$ density and (d–f) $N_2^+(B^2\Sigma_u^+)$ density due to a single sprite streamer with a driving current of 5 ms (Figures 9a–9d), 50 ms (Figures 9b–9e), and 100 ms (Figures 9c–9f).

3.2.3. $N_2^+(A^2\Pi_u)$ and $N_2^+(B^2\Sigma_u^+)$

Figures 9a–9c show the altitude and time dependence of the density of the $N_2^+(A^2\Pi_u)$ ion, responsible for the Meinel band emission, in the red and near-infrared spectral regions. Its behavior is similar to that of the reduced electric field shown in Figures 4a–4c. Due to the streamer head field, the concentration of $N_2^+(A^2\Pi_u)$ increases a magnitude between 10^5 cm^{-3} and 10^1 cm^{-3} at, respectively, 50 km and 80 km of altitude due to direct electron impact ionization of N_2:

$$P24 : e + N_2 \rightarrow N_2^+(A^2\Pi_u) + e + e.$$

$N_2^+(A^2\Pi_u)$ remains constant during the high-field phase due to the chemical balance between P24 and the collisional deexcitation process

$$P248 : N_2^+(A^2\Pi_u) + N_2 \rightarrow N_2^+ + N_2.$$

Below 65 km, and in the cases of 50 ms and 100 ms of current duration (see Figures 9b and 9c), the concentration of $N_2^+(A^2\Pi_u)$ reaches values close to 10^3 cm^{-3} due to the reduced electric field oscillations. The evolution of the electronically excited $N_2^+(B^2\Sigma_u^+)$ ion is similar to the one of the previously discussed species (see Figures 9d–9f). At 50 km of altitude the $N_2^+(B^2\Sigma_u^+)$ concentration reaches values close to 10^4 cm^{-3}, and at 80 km, it reaches just 10^{-3} cm^{-3}. At low altitudes this behavior is due to direct electron impact ionization of N_2

$$P23 : e + N_2 \rightarrow N_2^+(B^2\Sigma_u^+) + e + e,$$

which is activated by a very high reduced electric field in the streamer head (see Figure 5). After the high-field phase, the $N_2^+(B^2\Sigma_u^+)$ density returns to ambient values by spontaneous radiative decay:

$$P716 : N_2^+(B^2\Sigma_u^+) \rightarrow N_2^+ + h\nu.$$

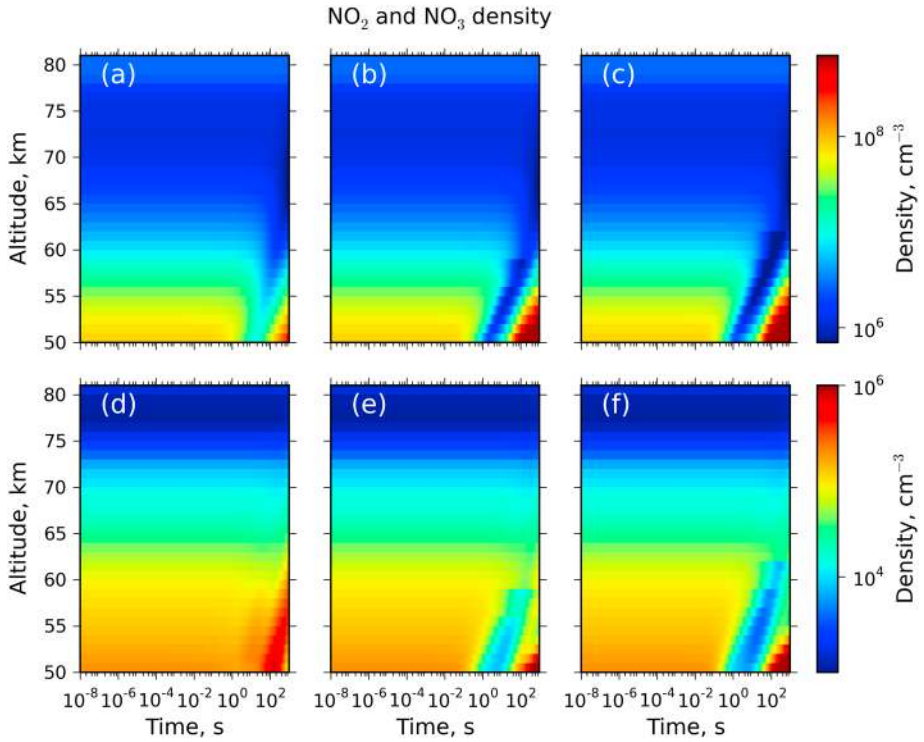

Figure 10. Altitude-time evolution of the (a–c) NO_2 density and (d–f) NO_3 density due to a single sprite streamer with a driving current of 5 ms (Figures 10a–10d), 50 ms (Figures 10e), and 100 ms (Figures 10f).

3.2.4. NO_2 and NO_3

The temporal evolution of the density of NO_2 at different altitudes for three different driving current durations investigated is shown in Figures 10a–10c. The impact of the streamer head and the high-field phase between 58 km and 80 km is negligible due to the balance of

$$P352 : O^- + NO \rightarrow NO_2 + e,$$

$$P411 : O + NO_3 \rightarrow NO_2 + O_2,$$

and

$$P413 : O + NO_2 \rightarrow O_2 + NO.$$

At low altitudes, we also see a constant NO_2 density due to the previous processes (P352 and P413), except P411, and

$$P368 : O_2^- + N \rightarrow NO_2 + e.$$

However, 0.1 s after the streamer head, the concentration of NO_2 decreases up to 1 order of magnitude because the detachment of O_2^- by N (P391) is less effective. Finally, at longer times, the density of NO_2 increases above its background value due to an enhanced ozone concentration at these times and the process

$$P418 : O_3 + NO \rightarrow NO_2 + O_2.$$

This NO_2 increase is proportional to the driving current duration.

The behavior of the NO_3 concentration (see Figures 10d–10f) is very similar to the previous case of NO_2. The NO_3 density is not affected by the streamer passage due to the balance between

$$P285 : NO_3^- + O_2^+ \rightarrow NO_3 + O + O,$$

and

$$P411 : NO_3 + O \rightarrow NO_2 + O_2.$$

For the case of the 5 ms driving current, below 60 km and starting approximately 10 s after the streamer head, we have small increases (up to a factor 4) due to the process P285. For the driving currents of 50 ms and 100 ms duration, and in the same way as for the NO_2 case, the density of NO_3 decreases between 59 km and 62 km almost 2 orders of magnitude 1 s after the streamer head due to the process P411. The concentration of NO_3 reverts to background values due to the increase of ozone and NO_2 densities for long times, which activate the process

$$P408 : NO_2 + O_3 \rightarrow NO_3 + O_2.$$

Due to the altitude at which sprites occur, we only have experimental data of their optical emissions that are proportional to the concentration of the excited emitting states. We can compare our results with previous models [i.e., *Sentman et al.*, 2008; *Gordillo-Vázquez*, 2008]. In the case of the nitrogen oxides we obtain different results and behaviors. This is mainly due to the use of different initial conditions and different reduced electric field characteristics. However, as in previous models, we obtain a higher impact in these species at low altitudes although our values are somewhat higher than in those models.

3.2.5. Metastable Excitations of Atomic Oxygen

The altitude and time dependence of the most important metastable excited species densities of atomic oxygen, i.e., $O(^1D)$ and $O(^1S)$, are shown in Figure 11. The concentration of the excited atomic oxygen $O(^1D)$, whose lifetime is 110 s, is shown in Figures 11a–11c. At high altitudes the behavior of the density of $O(^1D)$ is very similar in the three cases studied: the density of $O(^1D)$ increases strongly in the streamer head and remains elevated during the high-field phase. The $O(^1D)$ density reaches values between 10^8 cm^{-3} at 50 km of altitude and 10^4 cm^{-3} at 80 km of altitude. These increases are due to electron impact dissociative excitation

$$P37 : e + O_2 \rightarrow O(^1D) + O + e.$$

After the high-field phase, the $O(^1D)$ density returns slowly to its background value through the quenching reactions

$$P207 : O(^1D) + N_2 \rightarrow O + N_2,$$

and

$$P208 : O(^1D) + N_2 \rightarrow N_2(v1) + O.$$

For the cases of 50 ms and 100 ms current duration and at altitudes below 65 km (see Figures 11b and 11c), there are fast variations in the $O(^1D)$ density between 10^{-3} s and 10^{-1} s associated to the reduced electric field oscillations acting during the afterglow. The reduced electric field oscillations increase the $O(^1D)$ concentration up to 10^8 cm^{-3} due to the direct electron impact dissociative excitation process P37.

Similar to $O(^1D)$, the $O(^1S)$ density, with a lifetime of 0.7 s, also increases strongly in the streamer head reaching about 10^7 cm^{-3} and 10^3 cm^{-3} at 50 km and 80 km of altitude, respectively (see Figures 11d–11f). The main processes responsible for these increases are the direct electron impact dissociative excitation during the passage of the streamer head and the quenching of $N_2(C^3\Pi_u)$ by O_2 during the afterglow

$$P38 : e + O_2 \rightarrow O(^1S) + O + e,$$

$$P188 : N_2(C^3\Pi_u) + O_2 \rightarrow O(^1S) + N_2 + O.$$

Above 75 km, the concentration of $O(^1S)$ maintains these values until 1 s due to process P188. Later, $O(^1S)$ slowly returns to its background density by collisional deexcitation with molecular oxygen:

$$P224 : O(^1S) + O_2 \rightarrow O + O_2.$$

For the cases of 50 ms and 100 ms driving current (see Figures 11e and 11f, respectively) we see a number of variations in the $O(^1S)$ density between 10^{-3} s and 10^{-1} s due to direct electron impact dissociative

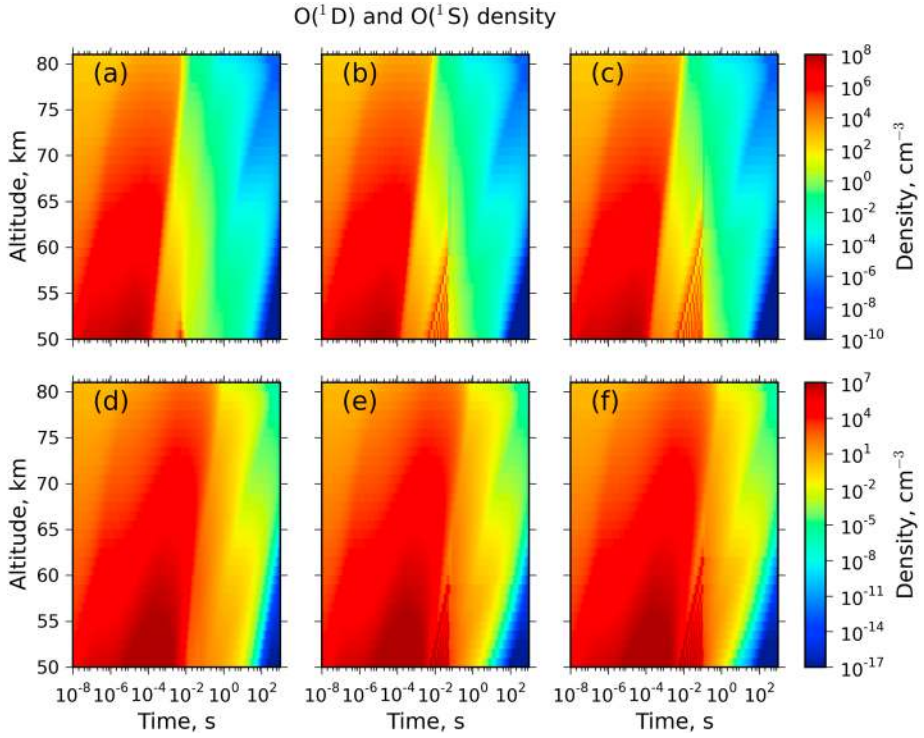

Figure 11. Altitude-time evolution of the (a–c) $O(^1D)$ density and (d–f) $O(^1S)$ density due to a single sprite streamer with a driving current of 5 ms (Figures 11a–11d), 50 ms (Figures 11b–11e), and 100 ms (Figures 11c–11f).

excitation of O_2 (P38). Recent measurements made by UARS [*Lee and Shepherd*, 2010] indicate sudden and significant 557.7 nm optical outbursts from $O(^1S)$ between 73 km and 87 km in coincidence with lightning flashes (or some seconds after lightning) that could have produced sprites in the upper atmosphere. The transient enhancement of the $O(^1S)$ concentration (and subsequent sudden optical outbursts) can be produced by electron impact dissociative excitation ($e + O_2 \rightarrow O + O(^1S) + e$) due to the abundant presence of energetic free electrons released by sprite streamer ionization events.

3.2.6. Atomic Oxygen and Ozone

The behavior of the ground state atomic oxygen concentration (see Figures 12a–12c) is very similar to the evolution of the NO density (see Figures 8d–8f). At the moment of the streamer head, the concentration of O increases between 10 orders of magnitude at 50 km of altitude and 1 order of magnitude at 80 km. This is produced by the direct electron impact dissociative excitation process (P37) of molecular oxygen. For longer times, the O density remains high due to the balance between quenching and dissociation:

$$P37 : e + O_2 \rightarrow O(^1D) + O + e,$$

$$P195 : N_2(A^3\Sigma_u^+) + O_2 \rightarrow N_2 + O + O,$$

$$P80 : e + O_3 \rightarrow O_2 + O + e,$$

and

$$P424 : O + O_2 + N_2 \rightarrow O_3 + N_2.$$

On the other hand, below 60 km the processes are

$$P193 : N_2(B^3\Pi_g) + O_2 \rightarrow N_2 + O + O,$$

$$P195 : N_2(A^3\Sigma_u^+) + O_2 \rightarrow N_2 + O + O,$$

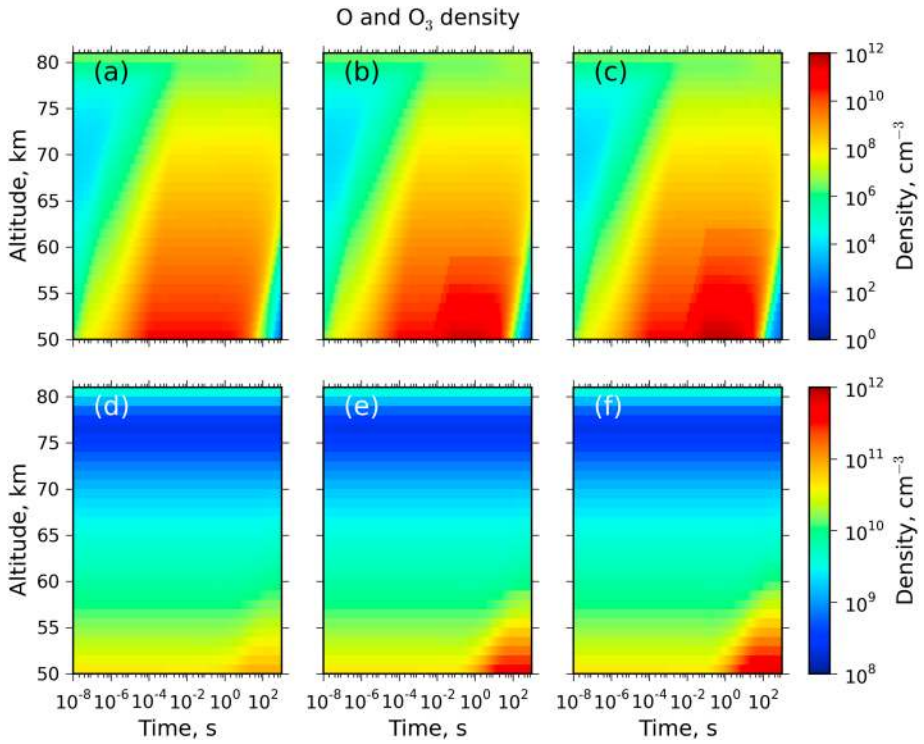

Figure 12. Altitude-time evolution of the (a–c) O density and (d–f) O_3 density due to a single sprite streamer with a driving current of 5 ms (Figures 12a–12d), 50 ms (Figures 12b–12e), and 100 ms (Figures 12c–12f).

$$P178 : N_2(a^1\Pi_g) + O_2 \rightarrow N_2 + O + O,$$

$$P80 : e + O_3 \rightarrow O_2 + O + e,$$

and

$$P424 : O + O_2 + N_2 \rightarrow O_3 + N_2,$$

which decrease the density of O starting 10 s after the streamer head. For the cases of 50 ms and 100 ms driving current (see Figures 12b and 12c, respectively), low altitudes and 10^{-2} s after the streamer head, the density of O increases through 1 order of magnitude by quenching of $N_2(B^3\Pi_g)$ by O_2 (P193) following the oscillations in the reduced electric field.

Looking now at ozone, Figures 12d–12f show that the O_3 density barely changes between 55 km and 80 km of altitude due to the balance between

$$P424 : O + O_2 + N_2 \rightarrow N_2 + O_3,$$

and

$$P80 : e + O_3 \rightarrow O_2 + O + e.$$

Below 56 km, there is an increase of O_3 by more than 1 order of magnitude for the case of 100 ms driving current (see Figure 12f) due to efficient three-body recombination of atomic oxygen (P424) at lower altitudes. This increase occurs 1 s after the streamer head because the electron density is too low and therefore the electron impact dissociation of O_3 (P80) is not as effective as the three-body recombination of O (P424).

3.2.7. Molecular Oxygen Metastables

We have also studied the metastables $O_2(a^1\Delta_g)$, with a lifetime of about 45 min, and $O_2(b^1\Sigma_g^+)$, with a lifetime of 12 s (see Figure 13). Regarding the first one, the $O_2(a^1\Delta_g)$ density shows a strong increase coinciding with the streamer head and reaches values close to 10^9 cm^{-3} and 10^6 cm^{-3} at, respectively, 50 km and 80 km of

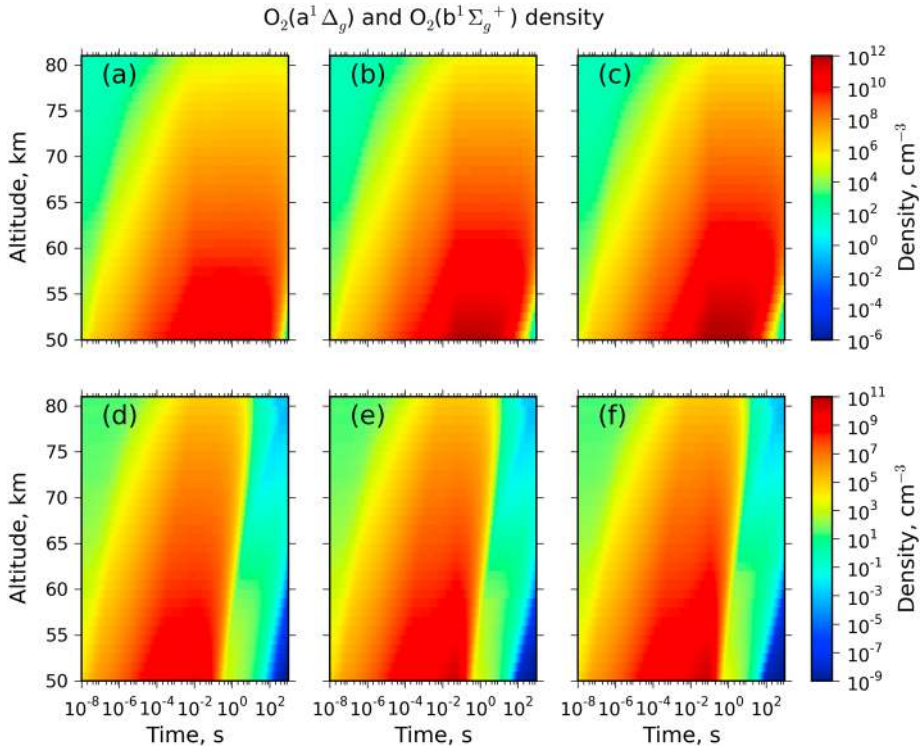

Figure 13. Altitude-time evolution of the (a–c) $O_2(a^1\Delta_g)$ density and (d–f) $O_2(b^1\Sigma_g^+)$ density due to a single sprite streamer with a driving current of 5 ms (Figures 13a–13d), 50 ms (Figures 13b–13e), and 100 ms (Figures 13c–13f).

altitude (see Figure 13a–13c). The main mechanism controlling the variation of $O_2(a^1\Delta_g)$ is direct electron impact excitation

$$P31 : e + O_2 \rightarrow O_2(a^1\Delta_g) + e.$$

After the production of $O_2(a^1\Delta_g)$ by P31, its high concentration persists due to the balance between

$$P241 : O_2(b^1\Sigma_g^+) + N_2 \rightarrow O_2(a^1\Delta_g) + N_2$$

and

$$P721 : O_2(a^1\Delta_g) \rightarrow O_2 + h\nu,$$

$$P236 : O_2(a^1\Delta_g) + O_2 \rightarrow O_2 + O_2.$$

Below 55 km, there is a secondary increase of $O_2(a^1\Delta_g)$ up to 10^{12} cm^{-3} (in the 100 ms case) due to the electron production by the oscillations of the electric field. Electrons accelerated by a high E/N produce $O_2(a^1\Delta_g)$ by direct electron impact excitation of O_2 (P31). At very long times (longer than 10^2 s), the $O_2(a^1\Delta_g)$ density tends to its ambient values due to collisional deexcitation with NO:

$$P240 : O_2(a^1\Delta_g) + NO \rightarrow NO + O_2.$$

The behavior of the mestastable $O_2(b^1\Sigma_g^+)$ is similar to that of $O_2(a^1\Delta_g)$. Figures 13d–13f show values, immediately after the streamer head, between 10^8 cm^{-3} and 10^6 cm^{-3} at 50 km and 80 km of altitude, respectively. As for $O_2(a^1\Delta_g)$, the main mechanism producing $O_2(b^1\Sigma_g^+)$ is direct electron impact excitation of O_2

$$P32 : e + O_2 \rightarrow O_2(b^1\Sigma_g^+) + e,$$

Above 60 km, the concentration of $O_2(b^1\Sigma_g^+)$ remains constant up to 1 s after it is produced. This is due to the balance between the processes

$$P209 : O(^1D) + O_2 \rightarrow O_2(b^1\Sigma_g^+) + O,$$

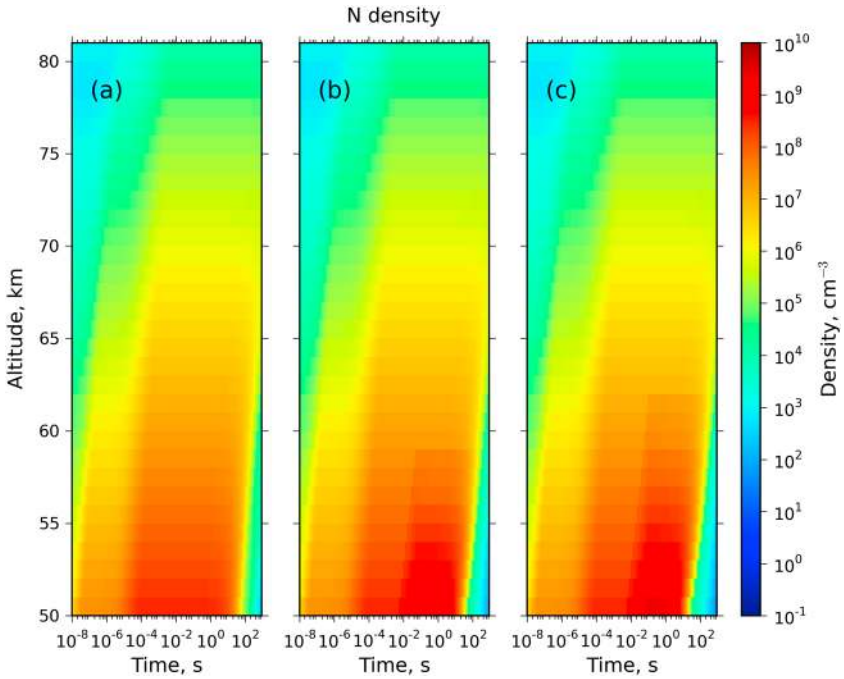

Figure 14. Altitude-time evolution of the atomic nitrogen density (N) due to a single sprite streamer with (a) 5 ms, (b) 50 ms, and (c) 100 ms driving current.

$$P206 : N_2(A^3\Sigma_u^+) + O_2 \rightarrow O_2(b^1\Sigma_g^+) + N_2,$$

and the reaction

$$P241 : O_2(b^1\Sigma_g^+) + N_2 \rightarrow O_2(a^1\Delta_g) + N_2.$$

The removal of $O_2(b^1\Sigma_g^+)$ is explained by the lowering of the electron density and the subsequent decrease of the density of $O(^1D)$ and $N_2(A^3\Sigma_u^+)$. For this reason, the quenching of $O_2(b^1\Sigma_g^+)$ by N_2 becomes more effective. Below 60 km, we see another increase of $O_2(b^1\Sigma_g^+)$ up to 10^{11} cm^{-3} for the cases of 50 ms and 100 ms driving current (see Figures 13e and 13f) due to the quenching of $O(^1D)$ by O_2 (P236).

3.2.8. Atomic Nitrogen

The evolution of the density of ground state nitrogen is shown in Figure 14. We can see how the N concentration increases by 7 orders of magnitude (up to 10^8 cm^{-3}) at 50 km at the moment of the streamer head and 2 orders of magnitude (up to 10^5 cm^{-3}) at 80 km. There is a further increase of 1 order of magnitude in the atomic nitrogen concentration during the high-field phase (between 10^{-5} and 10^{-4} s). The underlying mechanism of this later enhancement of N is the direct electron impact dissociative excitation of N_2:

$$P25 : e + N_2 \rightarrow N(^2D) + N + e.$$

The N density remains high during a long time, e.g., up to 10 s (at 50 km) due to the balance between

$$P171 : N(^2D) + N_2 \rightarrow N + N_2,$$

$$P180 : N_2(a^1\Pi_g) + NO \rightarrow N_2 + N + O,$$

$$P274 : O_2^- + NO^+ \rightarrow O_2 + N + O,$$

$$P100 : e + NO^+ \rightarrow N + O,$$

and

$$P395 : N + O_2 \rightarrow NO + O.$$

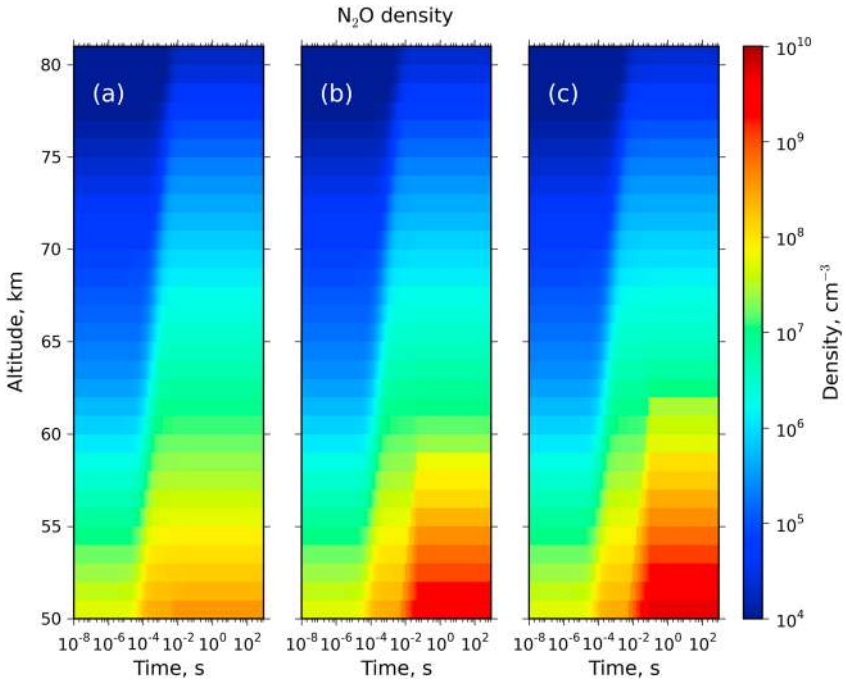

Figure 15. Altitude-time evolution of the N_2O density due to a single sprite streamer with (a) 5 ms, (b) 50 ms, and (c) 100 ms driving current.

Above 67 km, a high concentration of N persists for more than 1000 s due to the balance between the processes P171, P100, and the process P395. For the cases of 50 ms and 100 ms driving current durations (see Figures 14b and 14c, respectively) and below about 62 km, the density of ground state N increases up to factor 5, driven by the oscillations of the reduced electric field. The cause of this secondary increase is the direct electron impact dissociative excitation of N_2 (P25).

3.2.9. N_2O

The altitude and time dependence of the density of N_2O (a greenhouse gas and a very important species in the ozone cycle) is shown in Figure 15. We see that after the streamer head, the N_2O density increases up to 1 order of magnitude due to associative detachment (AD) of O^- by N_2:

$$P346 : O^- + N_2 \rightarrow N_2O + e.$$

As we have previously discussed, this process (P346) strongly depends on the reduced electric field. The N_2O density remains at these enhanced values during all the simulation due to the AD process together with

$$P397 : N + NO_2 \rightarrow N_2O + O,$$

and

$$P83 : e + N_2O \rightarrow N_2 + O + e,$$

$$P353 : O^- + N_2O \rightarrow NO^- + NO.$$

In a similar way but at altitudes above 75 km, the concentration of N_2O increases by a factor 6 due to AD and remains high due to the balance between AD, P397, P353,

$$P200 : N_2(A^3\Sigma_u^+) + N_2O \rightarrow NO + N_2 + N.$$

We also see in Figures 15b and 15c (50 ms and 100 ms driving current, respectively) that the N_2O density grows one additional order of magnitude due to the influence of the reduced electric field oscillations on the AD process of O^- by N_2 at low altitudes (below 62 km in the case of 100 ms current afterglow).

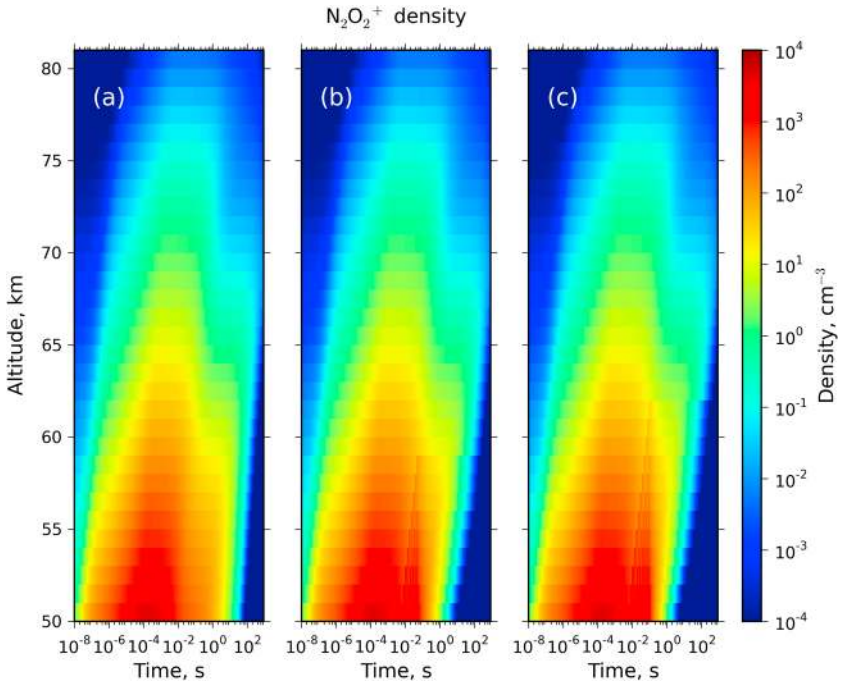

Figure 16. Altitude-time evolution of the $N_2O_2^+$ ion density due to a single sprite streamer with (a) 5 ms, (b) 50 ms, and (c) 100 ms driving current.

3.2.10. $N_2O_2^+$

The concentration of $N_2O_2^+$ ions at the moment of the streamer head passage exhibits a sharp increase of 8 orders of magnitude at low altitudes (see Figure 16). The $N_2O_2^+$ density also shows a smooth increase of one additional order of magnitude following the high-field phase. Both increases of the concentration of $N_2O_2^+$ are produced by three-body associative recombination

$$P335 : O_2^+ + N_2 + N_2 \rightarrow N_2O_2^+ + N_2.$$

Afterward, it decays toward to its ambient value due to dissociative recombination:

$$P345 : N_2O_2^+ + O_2 \rightarrow O_4^+ + N_2,$$

$$P344 : N_2O_2^+ + N_2 \rightarrow O_2^+ + N_2 + N_2.$$

Above 75 km, the concentration of $N_2O_2^+$ increases up to 4 orders of magnitude by the three-body associative recombination P335 but then slowly returns to its initial value due to dissociative recombination (P345). For the cases of 50 ms and 100 ms driving current (see Figures 16b and 16c, respectively) and below 60 km, the concentration of $N_2O_2^+$ barely changes during the oscillations of the reduced electric field oscillations.

3.2.11. $N_2(A^3\Sigma_u^+)$

The time evolution of the metastable $N_2(A^3\Sigma_u^+)$ density is shown in Figure 17. The behavior of the $N_2(A^3\Sigma_u^+)$ concentration is very similar to that of the reduced electric field (see Figures 4a–4c). Below 60 km, it increases sharply to 10^8 cm^{-3} at the moment of the streamer head due to direct electron impact excitation

$$P11 : e + N_2 \rightarrow N_2(A^3\Sigma_u^+) + e,$$

Later, the elevated density persists due to the spontaneous decay of $N_2(B^3\Pi_g)$

$$P703 : N_2(B^3\Pi_g) \rightarrow N_2(A^3\Sigma_u^+) + h\nu.$$

The density of $N_2(A^3\Sigma_u^+)$ finally returns to initial ambient values due to quenching with O_2 when the reduced electric field vanishes:

$$P195 : N_2(A^3\Sigma_u^+) + O_2 \rightarrow N_2 + O + O.$$

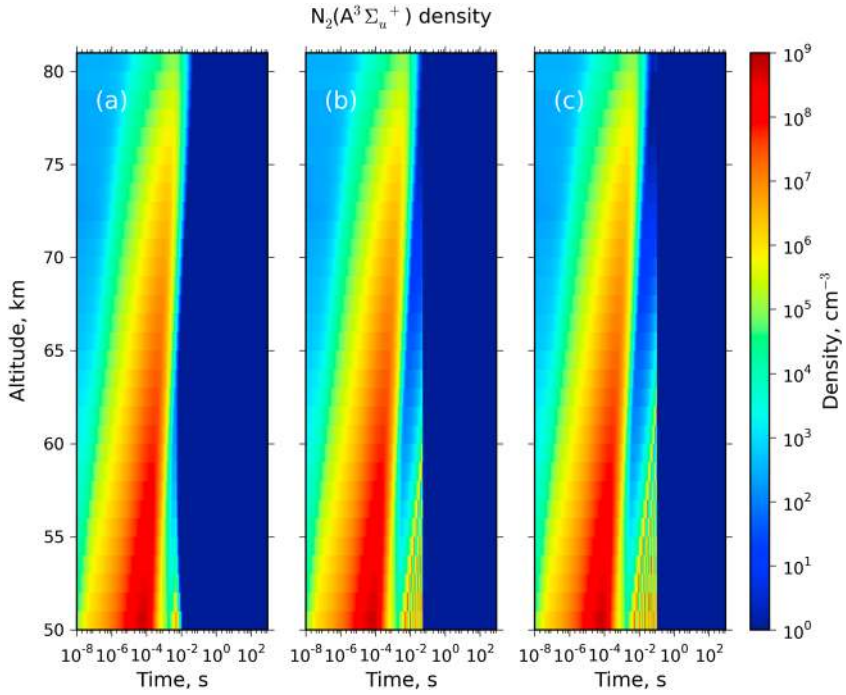

Figure 17. Altitude-time evolution of the metastable $N_2(A^3\Sigma_u^+)$ density due to a single sprite streamer with (a) 5 ms, (b) 50 ms, and (c) 100 ms driving current.

Above 75 km, the density of $N_2(A^3\Sigma_u^+)$ increases smoothly to about 10^6 cm^{-3} due to the spontaneous radiative decay of $N_2(B^3\Pi_g)$ to $N_2(A^3\Sigma_u^+)$. For the cases of 50 ms and 100 ms durations of the current (see Figures 17b and 17c, respectively) we have fast variations in the $N_2(A^3\Sigma_u^+)$ density associated to the reduced electric field oscillations, and the $N_2(A^3\Sigma_u^+)$ density reaches its maximum at the streamer head. These fast variations are caused by

$$P192 : N_2(B^3\Pi_g) + N_2 \rightarrow N_2(A^3\Sigma_u^+) + N_2,$$

$$P703 : N_2(B^3\Pi_g) \rightarrow N_2(A^3\Sigma_u^+) + h\nu,$$

$$P11 : e + N_2 \rightarrow N_2(A^3\Sigma_u^+) + e,$$

and

$$P195 : N_2(A^3\Sigma_u^+) + O_2 \rightarrow N_2 + O + O.$$

3.3. Optical Emission Brightness

In this section we will show and discuss the results of the optical emission brightness of the first and second positive band systems of N_2 as well as the NIR (near-infrared) emission brightness of the Meinel band of N_2^+ and those of the 4.26 μm and 14.9 μm IR bands of CO_2 under the action of single sprite streamer. As in the previous section, we have used three different driving current durations (53 ms, 50 ms, and 100 ms) to study the possible detection scenarios at different altitudes using suitable instrumentation. The emission brightness measured in Rayleighs ($1R = 10^6$ photons cm^{-2} s^{-1}) is calculated through the expression

$$EB(R) = 10^{-6} \int V(l)\mathrm{d}l, \tag{14}$$

where $V(l)$ is the so-called volume emission rate (in photons cm^{-3} s^{-1}) and the integral is taken along the line of sight through the emission volume over a characteristic length l. In our case, the magnitude l is the diameter of a sprite streamer, and we have considered the value of ~500 m [*Stenbaek-Nielsen et al.*, 2013] at 76 km, rescaled with the inverse of the density (for each altitude). The volume emission rate $V(l)$ is A_{ij} (s^{-1}) × N_i (cm^{-3}), that is, the product of the Einstein coefficients (A_{ij}) for spontaneous emission times the concentration of the i emitting excited state density (N_i).

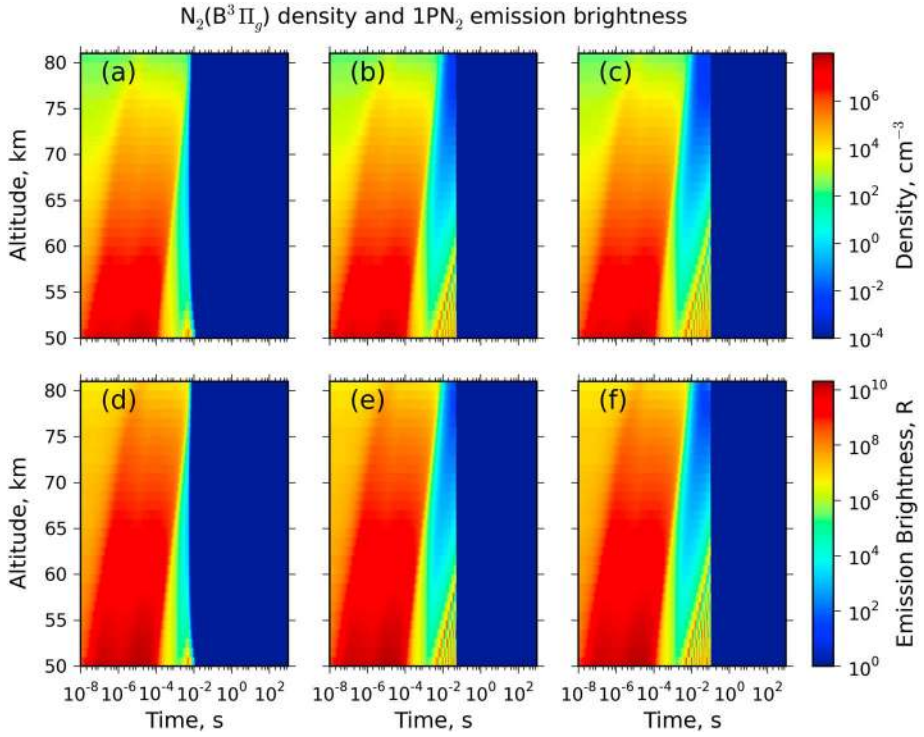

Figure 18. Altitude-time evolution of the (a–c) $N_2(B^3\Pi_g)$ density and (d–f) the first positive band system ($1PN_2$) emission brightness due to a single sprite streamer with a driving current of 5 ms (Figures 18a–18d), 50 ms (Figures 18b–18e), and 100 ms (Figures 18c–18f).

In Figures 18a–18c we can see the time evolution of the $N_2(B^3\Pi_g)$ density, whose radiative decay to $N_2(A^3\Sigma_u^+)$ is responsible for the first positive band system ($1PN_2$) of N_2. The emission brightness (EB) of the $1PN_2$ is shown in Figures 18d–18f. The EB of the $1PN_2$ exceeds 1 MR in almost all altitudes considered. This high brightness is produced by the strong $N_2(B^3\Pi_g)$ excitation in the streamer head and during the afterglow by, respectively, direct electron impact excitation

$$P15 : e + N_2 \rightarrow N_2(B^3\Pi_g) + e$$

and

$$P704 : N_2(C^3\Pi_u) \rightarrow N_2(B^3\Pi_g) + h\nu,$$

The main deexcitation mechanism of $N_2(B^3\Pi_g)$ is, at high altitudes, quenching by O_2

$$P193 : N_2(B^3\Pi_g) + O_2 \rightarrow N_2 + O + O,$$

and, at low altitudes, the radiative decay responsible for the $1PN_2$ emission

$$P703 : N_2(B^3\Pi_g) \rightarrow N_2(A^3\Sigma_u^+) + h\nu,$$

At very low altitudes (between 55 km and 50 km), the brightness of the reddish emission of $1PN_2$ can exceed 10 GR. The variations in the emission brightness (and therefore in the density of $N_2(B^3\Pi_g)$) are associated to the reduced electric field oscillations.

The behavior of the $2PN_2$ emission brightness (see Figure 19) is very similar to that of $1PN_1$. In this case, the EB also exceeds 1 MR in almost all the altitudes for the three cases considered due to the strong increase of the $N_2(C^3\Pi_u)$ density by electron impact excitation

$$P17 : e + N_2 \rightarrow N_2(C^3\Pi_u) + e$$

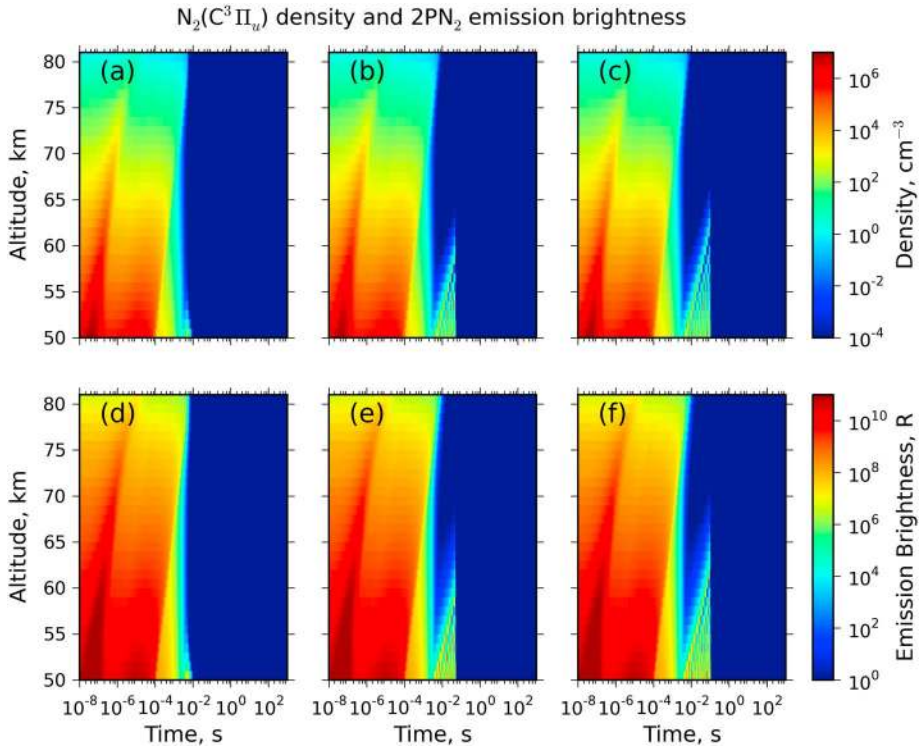

Figure 19. Altitude-time evolution of (a–c) the $N_2(C^3\Pi_u)$ density and (d–f) the second positive band system ($2PN_2$) emission brightness due to a single sprite streamer with a driving current of 5 ms (Figures 19a–19d), 50 ms (Figures 19b–19e), and 100 ms (Figures 19c–19f).

and its subsequent radiative decay

$$P704 : N_2(C^3\Pi_u) \rightarrow N_2(B^3\Pi_g) + h\nu.$$

Similar to the previous case, at low altitudes, the EB of the $2PN_2$ can exceed 10 GR for the blue emission corresponding to $2PN_2$.

In Figures 20a–20c, we can see that the IR (4.26 μm) emission brightness predicted by the present kinetic model simulations can also exceed 1 MR below 75 km of altitude for the case of 100 ms driving current (reaching 100 GR at 50 km) and below 70 km of altitude for the case of 5 ms driving current (exceeding 1 GR at 50 km). Just before the end of the driving current, the IR (4.26 μm) emission begins to increase due to the radiative deexcitation from $CO_2(00^01)$ to the fundamental state $CO_2(00^00)$.

$$P594 : CO_2(00^01) \rightarrow CO_2(00^00) + h\nu\ (4.26\mu m).$$

In order to achieve this strong IR emission, a high rate of $CO_2(00^01)$ production is necessary, being the direct electron impact vibrational excitation of CO_2 the main production mechanism of $CO_2(00^01)$ during the first stages of the emission

$$P48 : e + CO_2 \rightarrow CO_2(00^01) + e,$$

while when the reduced electric field falls to negligible values, the production of $CO_2(00^01)$ is dominated by the vibrational-vibrational process

$$P572 : N_2(v2) + CO_2(00^00) \rightarrow N_2(v1) + CO_2(00^01).$$

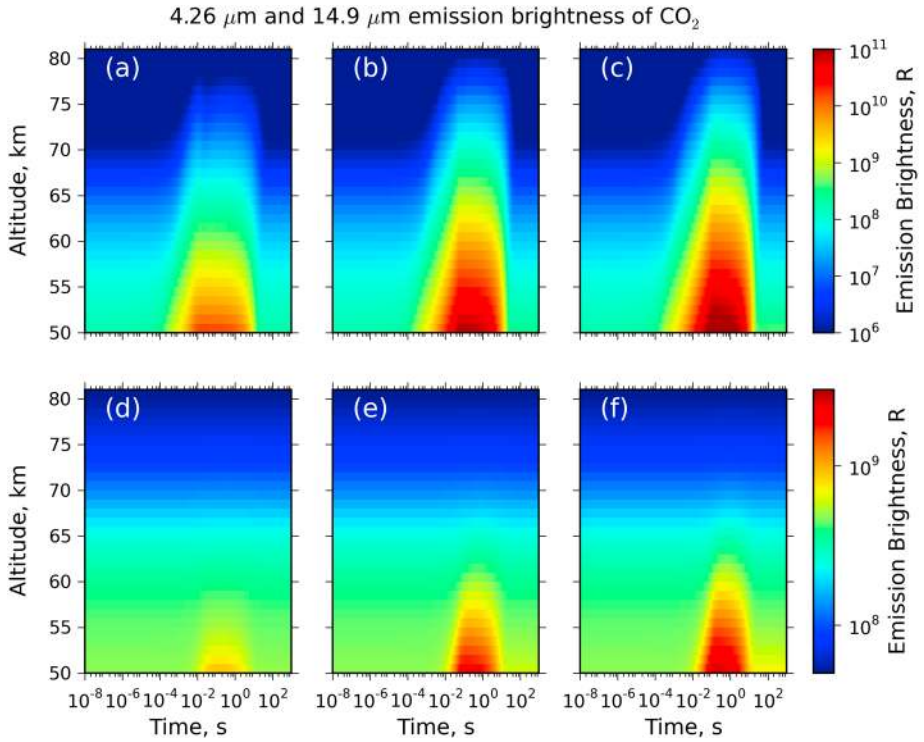

Figure 20. Altitude-time evolution of the (a–c) 4.26 μm and (d–f) 14.9 μm infrared emission brightness of CO_2 due to a single sprite streamer with a driving current of 5 ms (Figures 20a–20d), 50 ms (Figures 20b–20e), and 100 ms (Figures 20c–20f).

However, for the IR emission brightness at 14.9 μm, it can reach values above 1 GR for low altitudes (< 60 km) only for the cases of 50 ms and 100 ms driving currents (see Figures 20e and 20f). This 14.9 μm emission is produced by the radiative decay of the first vibrationally excited state of CO_2 to the ground state

$$P579 : CO_2(01^10) \rightarrow CO_2(00^00) + h\nu \ (14.9\mu m).$$

The production of $CO_2(01^10)$, necessary for the 14.9 μm IR emission, is dominated by vibrational-translational (VT) and vibrational-vibrational (VV) processes whose initial vibrationally excited states have been generated by electron impact excitation. The sum of several VT processes explains the increase of the $CO_2(01^10)$ density:

$$P485 : N_2 + CO_2(00^00) \rightarrow N_2 + CO_2(01^10),$$

$$P486 : N_2 + CO_2(02^00) \rightarrow N_2 + CO_2(01^10),$$

$$P487 : N_2 + CO_2(02^20) \rightarrow N_2 + CO_2(01^10),$$

together with the VV processes

$$P533 : CO_2(00^00) + CO_2(03^10) \rightarrow CO_2(02^00) + CO_2(01^10),$$

and

$$P534 : CO_2(00^00) + CO_2(03^10) \rightarrow CO_2(02^20) + CO_2(01^10).$$

The main loss mechanisms of $CO_2(01^10)$ are radiative decay (P579) and quenching of $CO_2(01^10)$ by N_2

$$P485 : N_2 + CO_2(01^10) \rightarrow N_2 + CO_2(00^00).$$

Considering now that the atmosphere, from mesosphere to space, behaves as optically thin, we think that the IR emissions associated to sprites could be detected with suitable space instrumentation pointing to the limb as in the case of LBH emissions [*Gordillo-Vázquez et al.*, 2011].

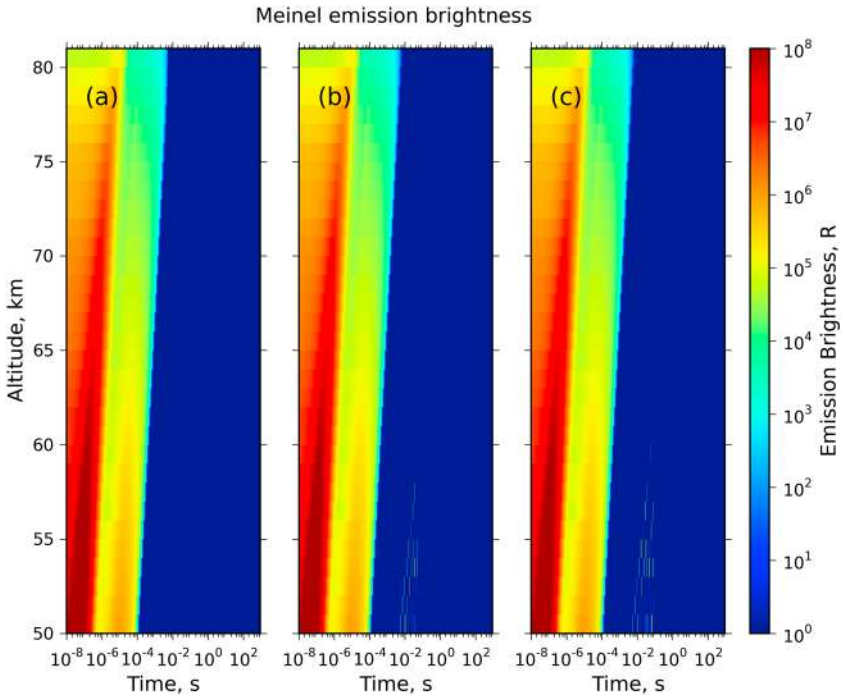

Figure 21. Altitude-time evolution of the Meinel ($N_2^+(A^2\Pi_u) \rightarrow N_2^+(X^2\Sigma_g^+)$) emission brightness due to a single sprite streamer with (a) 5 ms, (b) 50 ms, and (c) 100 ms driving current.

Finally, we show in Figure 21 the Meinel emission brightness due to a single sprite streamer for different driving current durations. Our model predicts, for the three cases studied (5 ms, 50 ms, and 100 ms), that the Meinel emission brightness does not reach 1 MR or barely reaches it at 50 km of altitude. Our predicted Meinel emission brightness grows with decreasing altitudes. Therefore, we speculate that the brightness due to Meinel emissions could reach and exceed 1 MR at tendrils altitudes and, consequently, the chances to detect it from ground or space platforms are small or none.

Figure 22 shows the altitude evolution of the possible detected number of photons per cm^{-2} per frame integration time as would be recorded by a camera of 33 fps (standard video rate) due a single sprite streamer with 50 ms driving current. We see in Figure 22 that the number of emitted photons per unit area of all the

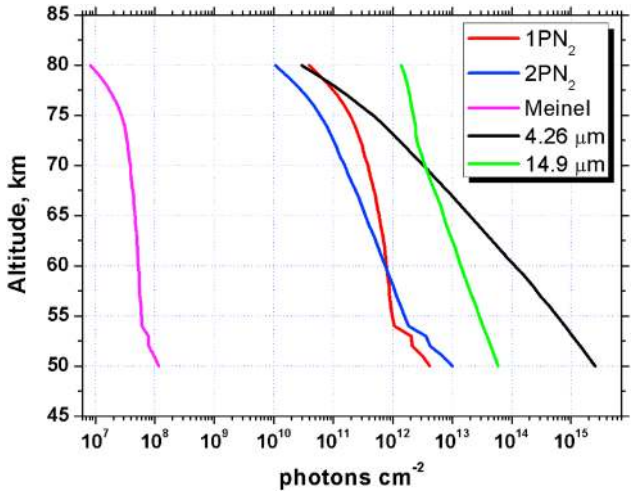

Figure 22. Altitude evolution of the detected number of photons per unit area per frame integration time due to a single sprite streamer with 50 ms driving current as would be measured by a 33 fps camera. The red, blue, and purple lines correspond, respectively, to the first and second positive band systems of N_2 and to the Meinel band of N_2^+. The black and green lines correspond to the 4.26 μm IR and 14.9 μm IR bands of CO_2.

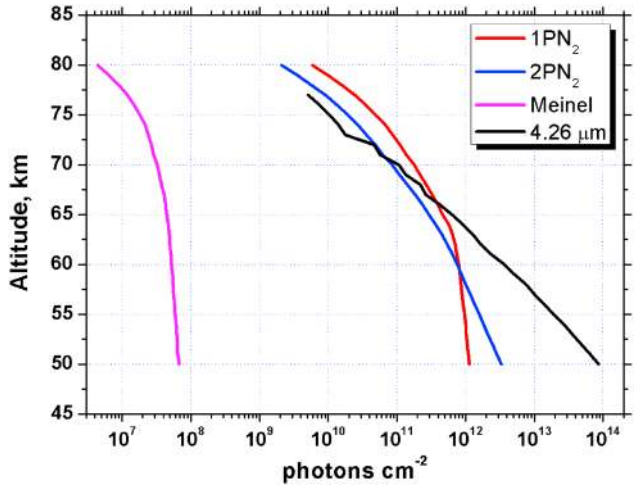

Figure 23. Altitude evolution of the detected number of photons per unit area per frame integration time due to a sprite streamer with 50 ms driving current as would be measured by a 1000 fps camera. The red, blue, and purple lines correspond, respectively, to the first and second positive band systems of N_2 and to the Meinel band of N_2^+. The black line corresponds to the 4.26 μm IR band of CO_2. In this case, we have not included the integrated number of photons per unit area of the 14.9 μm IR band because our model does not have sufficient temporal resolution at these timescales.

bands studied is above 10^{10} photons cm^{-2} (except for the Meinel band) in our model most reliable altitude range (70–80 km of altitude). It is also interesting to note that the CO_2 IR number of emitted photons per unit area (4.26 μm and 14.9 μm) could even exceed values of 10^{13} photons cm^{-2} between 60 and 50 km. The possibility of detection of sprite infrared emissions from space depends basically on the characteristics of the instrumentation. Even so, if we consider an optically thin atmosphere above 50 km, the infrared absoption is negligible. The emission brightness of the 4.26 μm band with respect the atmospheric background could be estimated through the ratio between the population of the $CO_2(00^01)$ after the streamer passage and the background population of the $CO_2(00^01)$. In this regard, the post streamer infrared emission brightness of the

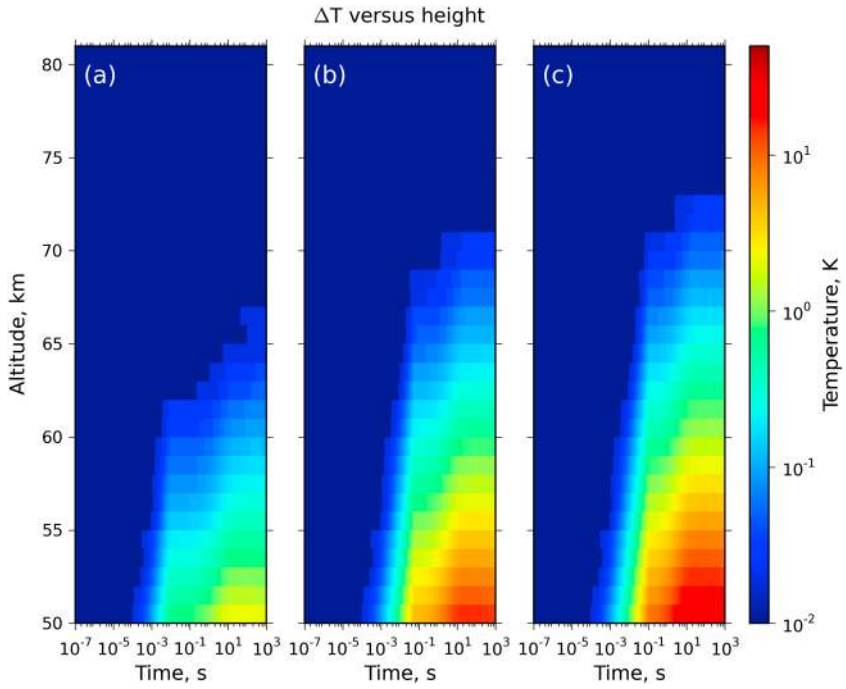

Figure 24. Altitude-time evolution of the gas temperature variation due to a single sprite streamer with (a) 5 ms, (b) 50 ms, and (c) 100 ms of driving current.

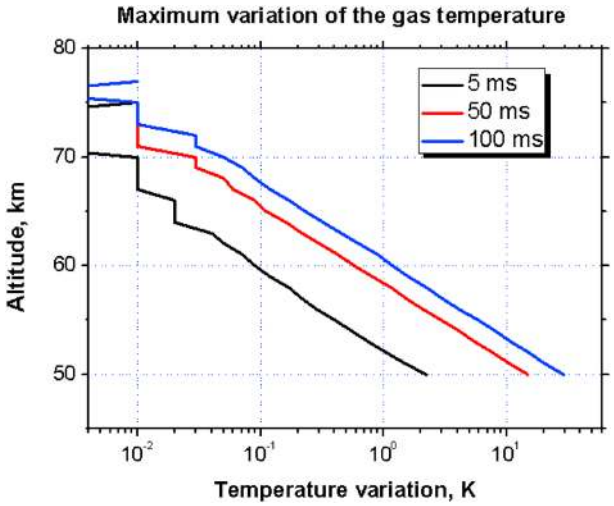

Figure 25. Altitude evolution of the maximum variation of the gas temperature. The solid black, red, and blue lines are for driving currents of, respectively, 5 ms, 50 ms, and 100 ms.

4.26 μm band is more than 2 orders of magnitude higher than the IR emission of the atmospheric background at 50 km and 1 order of magnitude higher at 65 km (see Figure 20).

In the same way, for the case of a camera recording at 1000 fps (see Figure 23) the detected number of photons per unit area of $1PN_2$, $2PN_2$, and 4.26 μm IR bands can exceed, according to our model, 10^{10} photons cm^{-2} below 75 km. As stated before, we need to be careful about our model results below 70 km since at these altitudes sprite streamers tend to branch and our model does not follow streamer branching dynamics.

As in the case of the nitrogen oxides, our emission brightness results disagree with previous models. We obtain higher values for the optical emission brightness than those reported by *Sentman et al.* [2008] and *Gordillo-Vázquez* [2008]. However, at altitudes between 68 km and 63 km, our calculations are in good agreement with the results by *Gordillo-Vázquez* [2008] for the N_2 second positive system band emission, which predict EB between 100 MR (68 km) and 10 GR (63 km). Finally, at 75 km, our model predicts sprite optical emissions between 10 MR and 1 GR for the first positive band system of N_2. These results agree, in the upper limit, with the observations reported by *Stenbaek-Nielsen et al.* [2007].

3.4. Thermal Impact

Finally, we discuss in this section the result shown in Figures 24a–24c in connection with the thermal impact of sprite streamers with 5 ms, 50 ms, and 100 ms driving current in the Earth's mesosphere. The most important increase in the gas temperature occurs at lower altitudes, between 60 km and 50 km, and it is proportional

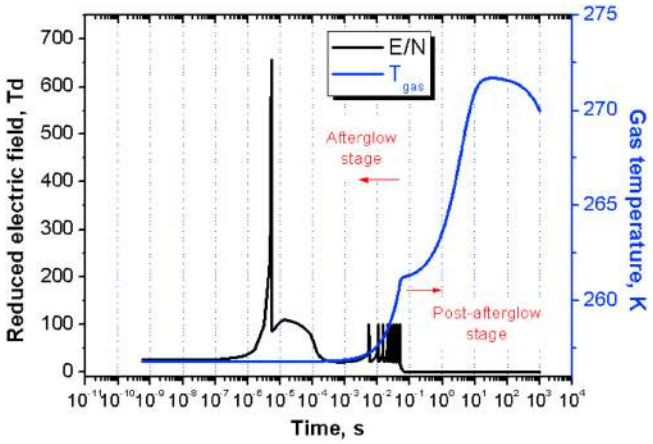

Figure 26. Temporal evolution of the gas temperature (blue line) and the reduced electric field (black line) at 50 km of altitude for the 50 ms driving current.

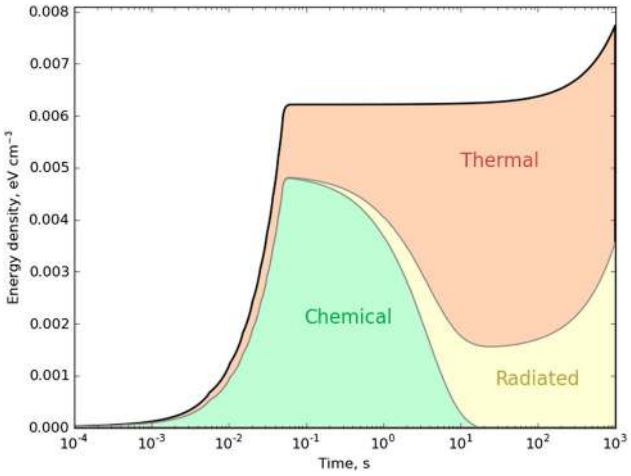

Figure 27. Time-dependent distribution of the energy density dissipated by a single sprite streamer with 50 ms driving current at an altitude of 50 km.

to the afterglow duration. At higher altitudes the variation of the gas temperature is negligible compared to that produced at lower layers.

We can see in Figure 25 the altitude evolution of the maximum variation of the gas temperature under the action of a sprite streamer. As previously discussed, the maximum gas temperature is reached at 50 km and it is strongly related with the duration of the driving current so that the temperature variation is greater for longer driving currents. The gas temperature maxima are 2.3 K, 15 K, and 29 K with 5 ms, 50 ms, and 100 ms driving currents, respectively.

The chemical mechanisms responsible for the gas heating are the same in the three cases studied, and consequently, we will only show from now on the results for the intermediate case (50 ms of afterglow) at 50 km of altitude. In Figure 26 we show the temporal evolution of the gas heating (blue line) and the reduced electric field (black line) at 50 km of altitude for the 50 ms afterglow case. We can see two different behaviors in the temporal evolution of the gas temperature related with the evolution of the reduced electric field. The first one is called "afterglow stage" and corresponds to the driving current, while the second one is called "postafterglow stage" and is related with the regime of negligible values taken by the reduced electric field between 54 ms and 33.6 s.

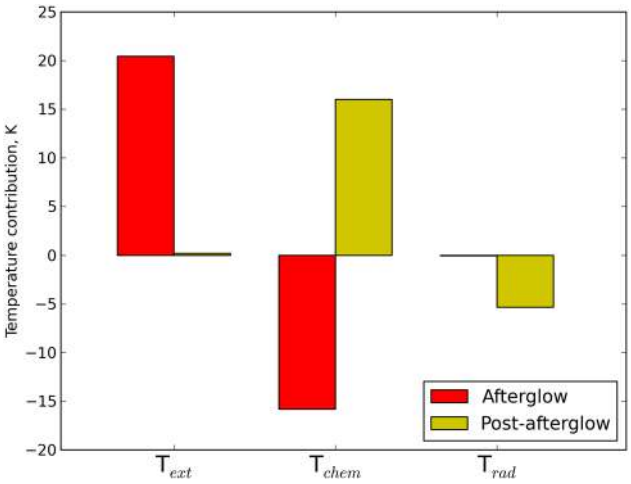

Figure 28. Time-integrated contribution to gas temperature of each energetic channel in the afterglow stage (red bars) and in the postafterglow stage (yellow bars) after the streamer head at 50 km of altitude and for the 50 ms driving current. Note that a negative sign of the temperature contribution corresponds to the temperature absorbed by the gas in nonthermal processes.

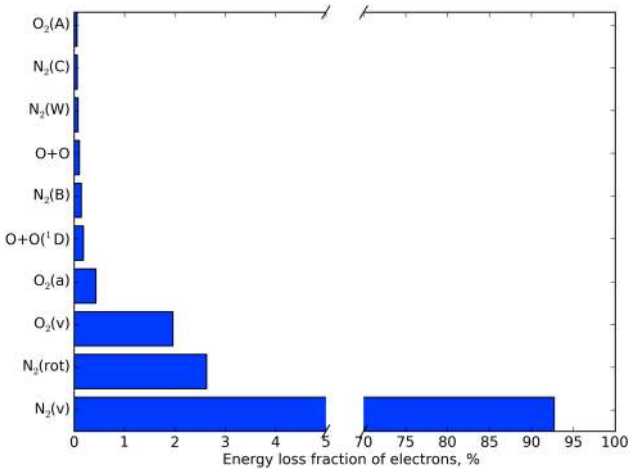

Figure 29. Electron energy loss fractions through electron impact collision producing the species above at 50 km of altitude for the 50 ms driving current. Note that in $O_2(v)$ and $N_2(v)$ we have taken into account all the vibrational levels considered.

Figure 27 shows the evolution of the energy contained in the gas under the action of a sprite streamer at 50 km of altitude. We can compare Figure 26 with Figure 27 for a better understanding of the energetic channels responsible for the gas heating. The red area in Figure 27 shows the total energy density imposed on the gas ($P_{ext} + P_{abs}$), the green area is the energy density of the chemical channel (P_{chem}), and the yellow area is the energy density corresponding with the radiative channel (P_{rad}). The electron energy channel P_{elec} is negligible. In the afterglow stage (up to 54 ms) the reduced electric field is the main mechanism injecting energy in the system being a large fraction of this electric field energy absorbed through the chemical channel. The difference between the energy density injected by the electric field and the energy density absorbed by the chemical processes is the net gas heating of the afterglow stage. When the reduced electric field goes to zero (postafterglow stage), the energy densities of the chemical and radiative channels decrease and the gas temperature increases again (see postafterglow stage in Figure 26).

From the thermal point of view, we can see in Figure 28 the time-integrated contribution of each channel to gas heating in the afterglow (red bars) and postafterglow (yellow bars) stages. We represent in Figure 28 the gas temperature variations produced by absorption/emission of external, chemical, and radiative power. We can note that, in the afterglow stage (up to 54 ms), the reduced electric field, through P_{ext}, produces an increase of more than 20 K (in the gas temperature). However, 15 K of those 20 K are deposited into the internal

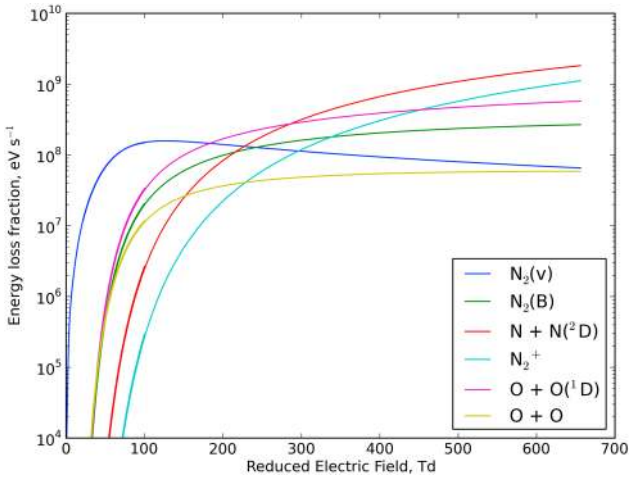

Figure 30. Fractions of electron energy partitioned into the excitation, ionization, and dissociation of molecules. These values are calculated at 50 km of altitude for the 50 ms driving current. Note that in $O_2(v)$ and $N_2(v)$ we have taken into account all the vibrational levels considered.

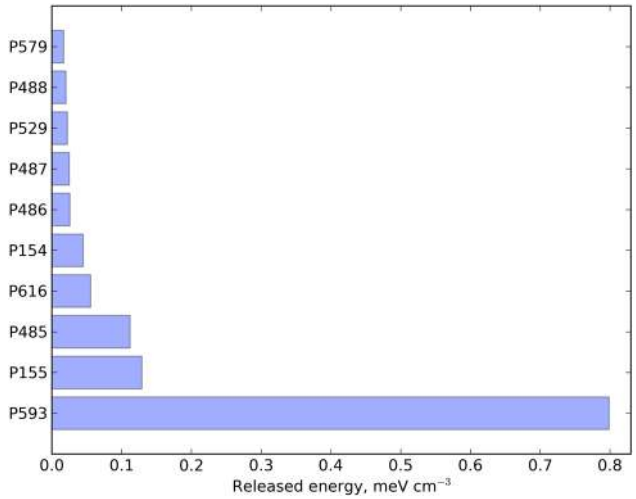

Figure 31. Time-integrated contribution of different kinetic processes to gas heating up to 33.6 s at 50 km of altitude for the 50 ms driving current.

degrees of freedom of the gas, i.e., P_{chem} (note that a negative sign of the temperature contribution in Figure 28 corresponds to the temperature absorbed by the gas in nonthermal processes). The temperature losses due to radiative decay are negligible (0.04 K) during afterglow. Therefore, the total (net) temperature increases in the afterglow stage is approximately of 4.5 K. The energy loss fraction of electrons by electron impact collisions in the afterglow stage is shown in Figure 29. Out of the 16 K deposited by the sprite streamer in P_{chem}, 92.7% goes to vibrational excitation of molecular nitrogen $N_2(v)$, 2.63% to rotational excitation of molecular nitrogen $N_2(rot)$, and 1.96% to vibrational excitation of molecular oxygen $O_2(v)$. This results is consistent with what we see in Figure 30, where we show the different energy loss fractions as a function of E/N for direct electron impact processes. The reduced electric field reached by the streamer head is approximately 650 Td (at 50 km of altitude) but for a very short time (of about several microseconds). However, the mean reduced electric field of all the sprite streamers E/N profile is below breakdown values, and consequently, direct electron impact vibrational excitation of N_2 is the main kinetic mechanism where the P_{chem} energy is stored.

Once the reduced electric field has dropped to negligible values, the P_{ext} channel only provides 0.2 K to the gas (see Figure 28, yellow bars) in the postafterglow stage. However, the external energy, mainly stored in the vibrational states of molecular nitrogen $N_2(v)$, is now transferred by vibrational-vibrational processes to $CO_2(v_1\ v_2^l\ v_3)$. The vibrational quenching of $CO_2(v_1\ v_2^l\ v_3)$ by N_2 and the radiative decay of vibrational excited CO_2 levels are the responsible for the ~11 K gas temperature increase during the postafterglow stage. The main processes underlying gas heating in the postafterglow stage are shown in Figure 31.

4. Conclusions

We have studied the electrical, chemical, and thermal impacts of a single sprite streamer with different driving current durations in the terrestrial mesosphere (50–80 km). In order to quantify the temporal evolution of each chemical species, our model solves a set of differential continuity equations for each of the chemical species considered (1) coupled with the Boltzmann equation (2), the Ohm law (10), and the energy conservation equation (9). Using as initial conditions the current density profiles provided for a set of altitudes by the streamer model by *Luque and Ebert* [2010], we have extended them using different constant driving current durations (5 ms, 50 ms, and 100 ms). For this, we have obtained the reduced electric field of a single sprite streamer for each of the altitudes considered so that the maximum current density occurs at the same time as the maximum reduced electric field. The constant driving current generates a high-field phase shorter than the driving current whose duration and value are, respectively, directly proportional to the altitude considered and close to breakdown (≃120 Td). At low altitudes and for the cases of 50 ms and 100 ms driving currents, we found a set of oscillations at the final stage of the E/N afterglow. We think that these undervoltage E/N oscillations built upon the opposite trends of electron production by associative detachment of O^- by N_2 and electron loss by dissociative recombination of electrons with O_4^+ during the driving current. At low altitudes, the electric field of the streamer head causes a huge growth in the electron

concentration up to 12 orders of magnitude (10^8 cm^{-3}) above ambient values. The tremendous increase in the electron concentration is driven by direct electron impact ionization of N_2 and O_2. In a similar way, the density of O^- exhibits a sharp enhancement past the streamer head due to dissociative attachment of O_2. Our model also predicts a quite significant enhancement in the concentration of metastable species ($N_2(A^3\Sigma_u^+)$, $O_2(a^1\Delta_g)$, $O_2(b^1\Sigma_g^+)$, $O(^1D)$, and $O(^1S)$) capable of storing energy for a relatively long time. The production of metastables is mainly caused by electron impact processes fueled by the high electron concentration caused by the streamer head electric field. We have also found an important (more than 2 orders of magnitude above ambient values at 50 km of altitude) and long-lasting (more than 10^3 s) enhancement of the N_2O density in the mesosphere. The presence of significant N_2O concentrations in the atmosphere for long times could substantially affect the ozone concentration. We have also evaluated the emission brightness of the first ($1PN_2$) and second ($2PN_2$) positive band systems of N_2 associated with key visible optical emissions of sprites, the CO_2 infrared emission at 4.26 μm and 14.9 μm, and the Meinel band of N_2^+ associated with red and near-infrared emissions. As expected, at low altitudes the reddish and bluish emission brightness of $1PN_2$ and $2PN_2$ exceed 1 MR by 4 orders of magnitude both at the streamer head and during the afterglow. In the same range of altitudes but at the final stages of the E/N afterglow, the 4.26 μm IR emission brightness can exceed 100 GR due to the high $CO_2(00^01)$ density production by electron impact collision and by VV processes involving $N_2(v)$. We think that this IR emission could be recorded from space detectors pointing toward the limb. Moreover, we found that the Meinel band emission brightness under the action of a single sprite streamer does not reach 1 MR at any altitude. However, we can conclude from our simulations that it could exceed 1 MR at tendril altitudes. Finally, our model predicts a relatively important increase in the temperature of the low altitude (< 65 km) atmosphere surrounding a single sprite streamer. This gas temperature enhancement increases at lower altitudes and depends directly on the duration of the driving current. A gas temperature increase ($\Delta T/T$) of up to ~ 6.1% could be reached at 50 km for the intermediate case considered (50 ms of driving current). This gas temperature enhancement is mainly caused by the collisional quenching of the vibrationally excited $CO_2(v_1\ v_2^l v_3)$ (previously excited through VV collisions with $N_2(v)$) with ground N_2 and, also, by the radiative decays of $CO_2(00^01)$ underlying the 4.26 μm IR emission. Future work will extend our simulations to blue jets at lower altitudes where our model predicts an important local heating in the atmosphere surrounding the TLE.

Acknowledgments

The kinetic model used in the simulations reported in the paper is available as supporting information. The full output can be requested from the corresponding author. This work was supported by the Spanish Ministry of Economy and Competitiveness, MINECO, under projects AYA2011-29936-C05-02 and ESP2013-48032-C5-5-R and by the Junta de Andalucía, Proyecto de Excelencia, FQM-5965. F.C.P.R. acknowledges MINECO for the FPI grant BES-2010-042367. A.L. was supported by a Ramón y Cajal contract, code RYC-2011-07801. We also acknowledge Maia Leire García Comas (IAA-CSIC) for providing CO_2 radiative decay data values and S. Pancheshnyi for enriching conversations about gas heating.

Michael Liemohn thanks two anonymous reviewers for their assistance in evaluating this paper.

References

Adachi, T., et al. (2006), Electric field transition between the diffuse and streamer regions of sprites estimated from ISUAL/array photometer measurements, *Geophys. Res. Lett.*, *33*, L17803, doi:10.1029/2006GL026495.

Adachi, T., et al. (2008), Electric fields and electron energies in sprites and temporal evolutions of lightning charge moment, *J. Phys. D*, *41*(23), 234010, doi:10.1088/0022-3727/41/23/234010.

Armstrong, R. A., J. A. Shorter, M. J. Taylor, D. M. Suszcynsky, W. A. Lyons, and L. S. Jeong (1998), Photometric measurements in the SPRITES '95 and '96 campaigns of nitrogen second positive (399.8 nm) and first negative (427.8 nm) emissions, *J. Atmos. Sol. Terr. Phys.*, *60*, 787–799, doi:10.1016/S1364-6826(98)00026-1.

Armstrong, R. A., D. M. Suszcynsky, W. A. Lyons, and T. E. Nelson (2000), Multi-color photometric measurements of ionization and energies in sprites, *Geophys. Res. Lett.*, *27*, 653–656, doi:10.1029/1999GL003672.

Arnone, E., et al. (2008), Seeking sprite-induced signatures in remotely sensed middle atmosphere NO_2, *Geophys. Res. Lett.*, *35*, L05807, doi:10.1029/2007GL031791.

Barrington-Leigh, C. P., U. S. Inan, M. Stanley, and S. A. Cummer (1999), Sprites triggered by negative lightning discharges, *Geophys. Res. Lett.*, *26*, 3605–3608, doi:10.1029/1999GL010692.

Barrington-Leigh, C. P., U. S. Inan, and M. Stanley (2001), Identification of sprites and elves with intensified video and broadband array photometry, *J. Geophys. Res.*, *106*, 1741–1750, doi:10.1029/2000JA000073.

Bell, T. F., V. P. Pasko, and U. S. Inan (1995), Runaway electrons as a source of Red Sprites in the mesosphere, *Geophys. Res. Lett.*, *22*, 2127–2130, doi:10.1029/95GL02239.

Bell, T. F., S. C. Reising, and U. S. Inan (1998), Intense continuing currents following positive cloud-to-ground lightning associated with red sprites, *Geophys. Res. Lett.*, *25*, 1285–1288, doi:10.1029/98GL00734.

Bering, E. A., III, et al. (2004), The results from the 1999 sprites balloon campaign, *Adv. Space Res.*, *34*, 1782–1791, doi:10.1016/j.asr.2003.05.043.

Bhusal, L., et al. (2004), Statistics and properties of transient luminous events found in the 1999 Sprites Balloon Campaign, *Adv. Space Res.*, *34*, 1811–1814, doi:10.1016/j.asr.2003.05.045.

Blanc, E., T. Farges, R. Roche, D. Brebion, T. Hua, A. Labarthe, and V. Melnikov (2004), Nadir observations of sprites from the International Space Station, *J. Geophys. Res.*, *109*, A02306, doi:10.1029/2003JA009972.

Boccippio, D. J., E. R. Williams, S. J. Heckman, W. A. Lyons, I. T. Baker, and R. Boldi (1995), Sprites, ELF transients, and positive ground strokes, *Science*, *269*, 1088–1091, doi:10.1126/science.269.5227.1088.

Boeck, W. L., O. H. Vaughan, R. J. Blakeslee, B. Vonnegut, M. Brook, and J. McKune (1995), Observations of lightning in the stratosphere, *J. Geophys. Res.*, *100*(D1), 1465–1475, doi:10.1029/94JD02432.

Boeck, W. L., O. H. Vaughan, R. J. Blakeslee, B. Vonnegut, and M. Brook (1998), The role of the space shuttle videotapes in the discovery of sprites, jets and elves, *J. Atmos. Sol. Terr. Phys.*, *60*, 669–677, doi:10.1016/S1364-6826(98)00025-X.

Bór, J. (2013), Optically perceptible characteristics of sprites observed in Central Europe in 2007–2009, *J. Atmos. Terr. Phys.*, *92*, 151–177, doi:10.1016/j.jastp.2012.10.008.

Bucsela, E., J. Morrill, M. Heavner, C. Siefring, S. Berg, D. Hampton, D. Moudry, E. Wescott, and D. Sentman (2003), $N_2(B^3\Pi_g)$ and $N_2^+(A^2\Pi_u)$ vibrational distributions observed in sprites, *J. Atmos. Sol. Terr. Phys.*, *65*, 583–590, doi:10.1016/S1364-6826(02)00316-4.

Chen, A. B., et al. (2008), Global distributions and occurrence rates of transient luminous events, *J. Geophys. Res.*, *113*, A08306, doi:10.1029/2008JA013101.

Cho, M., and M. J. Rycroft (1998), Computer simulation of the electric field structure and optical emission from cloud-top to the ionosphere, *J. Atmos. Sol. Terr. Phys.*, *60*, 871–888, doi:10.1016/S1364-6826(98)00017-0.

Cummer, S. A., and M. Füllekrug (2001), Unusually intense continuing current in lightning produces delayed mesospheric breakdown, *Geophys. Res. Lett.*, *28*, 495–498, doi:10.1029/2000GL012214.

Cummer, S. A., N. Jaugey, J. Li, W. A. Lyons, T. E. Nelson, and E. A. Gerken (2006), Submillisecond imaging of sprite development and structure, *Geophys. Res. Lett.*, *33*, L04104, doi:10.1029/2005GL024969.

da Silva, C. L., and V. P. Pasko (2014), Infrasonic acoustic waves generated by fast air heating in sprite cores, *Geophys. Res. Lett.*, *41*, 1789–1795, doi:10.1002/2013GL059164.

Enell, C.-F., et al. (2008), Parameterisation of the chemical effect of sprites in the middle atmosphere, *Ann. Geophys.*, *26*, 13–27, doi:10.5194/angeo-26-13-2008.

Evtushenko, A. A., F. A. Kuterin, and E. A. Mareev (2013), A model of sprite influence on the chemical balance of mesosphere, *J. Atmos. Terr. Phys.*, *102*, 298–310, doi:10.1016/j.jastp.2013.06.005.

Farges, T., E. Blanc, A. Le Pichon, T. Neubert, and T. H. Allin (2005), Identification of infrasound produced by sprites during the Sprite2003 campaign, *Geophys. Res. Lett.*, *32*, L01813, doi:10.1029/2004GL021212.

Franz, R. C., R. J. Nemzek, and J. R. Winckler (1990), Television image of a large upward electrical discharge above a thunderstorm system, *Science*, *249*, 48–51, doi:10.1126/science.249.4964.48.

Füllekrug, M., R. Roussel-Dupré, E. M. D. Symbalisty, O. Chanrion, A. Odzimek, O. van der Velde, and T. Neubert (2010), Relativistic runaway breakdown in low-frequency radio, *J. Geophys. Res.*, *115*, A00E09, doi:10.1029/2009JA014468.

Gerken, E., and U. Inan (2005), Streamers and diffuse glow observed in upper atmospheric electrical discharges, *IEEE Trans. Plasma Sci.*, *33*, 282–283, doi:10.1109/TPS.2005.845010.

Gerken, E. A., and U. S. Inan (2003), Observations of decameter-scale morphologies in sprites, *J. Atmos. Sol. Terr. Phys.*, *65*, 567–572, doi:10.1016/S1364-6826(02)00333-4.

Gerken, E. A., U. S. Inan, and C. P. Barrington-Leigh (2000), Telescopic imaging of sprites, *Geophys. Res. Lett.*, *27*, 2637–2640, doi:10.1029/2000GL000035.

Gordillo-Vázquez, F. J. (2008), Air plasma kinetics under the influence of sprites, *J. Phys. D*, *41*(23), 234016, doi:10.1088/0022-3727/41/23/234016.

Gordillo-Vázquez, F. J. (2010), Vibrational kinetics of air plasmas induced by sprites, *J. Geophys. Res.*, *115*, A00E25, doi:10.1029/2009JA014688.

Gordillo-Vázquez, F. J., and A. Luque (2010), Electrical conductivity in sprite streamer channels, *Geophys. Res. Lett.*, *37*, L16809, doi:10.1029/2010GL044349.

Gordillo-Vázquez, F. J., A. Luque, and M. Simek (2011), Spectrum of sprite halos, *J. Geophys. Res.*, *116*, A09319, doi:10.1029/2011JA016652.

Gordillo-Vázquez, F. J., A. Luque, and M. Simek (2012), Near infrared and ultraviolet spectra of TLEs, *J. Geophys. Res.*, *117*, A05239, doi:10.1029/2012JA017516.

Hagelaar, G. J. M., and L. C. Pitchford (2005), Solving the Boltzmann equation to obtain electron transport coefficients and rate coefficients for fluid models, *Plasma Sources Sci. Technol.*, *14*, 722, doi:10.1088/0963-0252/14/4/011.

Hampton, D. L., M. J. Heavner, E. M. Wescott, and D. D. Sentman (1996), Optical spectral characteristics of sprites, *Geophys. Res. Lett.*, *23*, 89–92, doi:10.1029/95GL03587.

Heavner, M. J. (2000), Optical spectroscopic observations of sprites, blue jets, and elves: Inferred microphysical processes and their macrophysical implications, PhD thesis, Univ. of Alaska, Fairbanks.

Heavner, M. J., J. S. Morrill, C. Siefring, D. D. Sentman, D. R. Moudry, E. M. Wescott, and E. J. Bucsela (2010), Near-ultraviolet and blue spectral observations of sprites in the 320–460 nm region: N_2 (2PG) emissions, *J. Geophys. Res.*, *115*, A00E44, doi:10.1029/2009JA014858.

Hiraki, Y., L. Tong, H. Fukunishi, K. Nanbu, Y. Kasai, and A. Ichimura (2004), Generation of metastable oxygen atom $O(^1D)$ in sprite halos, *Geophys. Res. Lett.*, *31*, L14105, doi:10.1029/2004GL020048.

Hiraki, Y., Y. Kasai, and H. Fukunishi (2008), Chemistry of sprite discharges through ion-neutral reactions, *Atmos. Chem. Phys.*, *8*, 3919–3928.

Hu, W., S. A. Cummer, and W. A. Lyons (2007), Testing sprite initiation theory using lightning measurements and modeled electromagnetic fields, *J. Geophys. Res.*, *112*, D13115, doi:10.1029/2006JD007939.

Jehl, A., T. Farges, and E. Blanc (2013), Color pictures of sprites from non-dedicated observation on board the International Space Station, *J. Geophys. Res. Space Physics*, *118*, 454–461, doi:10.1029/2012JA018144.

Kumar, S., A. Kumar, and C. J. Rodger (2008), Subionospheric early VLF perturbations observed at Suva: VLF detection of red sprites in the day?*J. Geophys. Res.*, *113*, A03311, doi:10.1029/2007JA012734.

Kuo, C.-L., R. R. Hsu, A. B. Chen, H. T. Su, L. C. Lee, S. B. Mende, H. U. Frey, H. Fukunishi, and Y. Takahashi (2005), Electric fields and electron energies inferred from the ISUAL recorded sprites, *Geophys. Res. Lett.*, *32*, L19103, doi:10.1029/2005GL023389.

Lee, Y. S., and G. G. Shepherd (2010), Summer high-latitude mesospheric observations of supersonic bursts and O(1S) emission rate with the UARS WINDII instrument and the association with sprites, meteors, and lightning, *J. Geophys. Res.*, *115*, A00E26, doi:10.1029/2009JA014731.

Liu, N. (2010), Model of sprite luminous trail caused by increasing streamer current, *Geophys. Res. Lett.*, *37*, L04102, doi:10.1029/2009GL042214.

Liu, N., and V. P. Pasko (2005), Molecular nitrogen LBH band system far-UV emissions of sprite streamers, *Geophys. Res. Lett.*, *32*, L05104, doi:10.1029/2004GL022001.

Liu, N., and V. P. Pasko (2007), Modeling studies of NO-γ emissions of sprites, *Geophys. Res. Lett.*, *34*, L16103, doi:10.1029/2007GL030352.

Liu, N., V. P. Pasko, H. U. Frey, S. B. Mende, H.-T. Su, A. B. Chen, R.-R. Hsu, and L.-C. Lee (2009), Assessment of sprite initiating electric fields and quenching altitude of $a^1\Pi_g$ state of N_2 using sprite streamer modeling and ISUAL spectrophotometric measurements, *J. Geophys. Res.*, *114*, A00E02, doi:10.1029/2008JA013735.

Liu, N., et al. (2006), Comparison of results from sprite streamer modeling with spectrophotometric measurements by ISUAL instrument on FORMOSAT-2 satellite, *Geophys. Res. Lett.*, *33*, L01101, doi:10.1029/2005GL024243.

López-Puertas, M. (1982), Emisiones del CO_2 en 4.26 y 15 μm en las atmósferas de los planetas interiores, PhD thesis, Universidad de Granada, Granada, Spain.

Luque, A., and U. Ebert (2010), Sprites in varying air density: Charge conservation, glowing negative trails and changing velocity, *Geophys. Res. Lett.*, *37*, L06806, doi:10.1029/2009GL041982.

Luque, A., and F. J. Gordillo-Vázquez (2011), Modeling and analysis of $N_2(B^3\Pi_g)$ and $N_2(C^3\Pi_u)$ vibrational distributions in sprites, *J. Geophys. Res.*, *116*, A02306, doi:10.1029/2010JA015952.

Luque, A., and F. J. Gordillo-Vázquez (2012), Mesospheric electric breakdown and delayed sprite ignition caused by electron detachment, *Nat. Geosci.*, *5*, 22–25, doi:10.1038/ngeo1314.

Luque, A., V. Ratushnaya, and U. Ebert (2008), Positive and negative streamers in ambient air: Modelling evolution and velocities, *J. Phys. D*, *41*(23), 234005, doi:10.1088/0022-3727/41/23/234005.

Lyons, W. A. (1996), Sprite observations above the U.S. High Plains in relation to their parent thunderstorm systems, *J. Geophys. Res.*, *101*, 29641–29652, doi:10.1029/96JD01866.

Marsh, D. R., M. J. Mills, D. E. Kinnison, J. F. Lamarque, N. Calvo, and L. M. Polvani (2013), Climate change from 1850 to 2005 simulated in CESM1 (WACCM), *J. Clim.*, *26*(19), 7372–7391, doi:10.1175/JCLI-D-12-00558.1.

Marshall, R. A., and U. S. Inan (2005), High-speed telescopic imaging of sprites, *Geophys. Res. Lett.*, *32*, L05804, doi:10.1029/2004GL021988.

Marshall, R. A., and U. S. Inan (2006), High-speed measurements of small-scale features in sprites: Sizes and lifetimes, *Radio Sci.*, *41*, RS6S43, doi:10.1029/2005RS003353.

McHarg, M. G., H. C. Stenbaek-Nielsen, and T. Kammae (2007), Observations of streamer formation in sprites, *Geophys. Res. Lett.*, *34*, L06804, doi:10.1029/2006GL027854.

Mende, S., H. Frey, R. R. Hsu, H. T. Su, A. Chen, L. C. Lee, H. Fukunishi, and Y. Takahashi (2004), Sprite imaging results from the ROCSAT-2 ISUAL instrument, *Eos Trans. AGU*, *85*(47), Fall Meet. Suppl., Abstract AE51A-02.

Mende, S. B., R. L. Rairden, G. R. Swenson, and W. A. Lyons (1995), Sprite spectra: N_2 1 PG band identification, *Geophys. Res. Lett.*, *22*, 2633–2636, doi:10.1029/95GL02827.

Mende, S. B., H. U. Frey, R. R. Hsu, H. T. Su, A. B. Chen, L. C. Lee, D. D. Sentman, Y. Takahashi, and H. Fukunishi (2005), D region ionization by lightning-induced electromagnetic pulses, *J. Geophys. Res.*, *110*, A11312, doi:10.1029/2005JA011064.

Milikh, G. M., D. A. Usikov, and J. A. Valdivia (1998), Model of infrared emission from sprites, *J. Atmos. Sol. Terr. Phys.*, *60*, 895–905, doi:10.1016/S1364-6826(98)80009-6.

Mishin, E. (1997), Ozone layer perturbation by a single blue jet, *Geophys. Res. Lett.*, *24*, 1919–1922, doi:10.1029/97GL01890.

Morrill, J., et al. (2002), Electron energy and electric field estimates in sprites derived from ionized and neutral N_2 emissions, *Geophys. Res. Lett.*, *29*(10), 1462, doi:10.1029/2001GL014018.

Morrill, J. S., E. J. Bucsela, V. P. Pasko, S. L. Berg, M. J. Heavner, D. R. Moudry, W. M. Benesch, E. M. Wescott, and D. D. Sentman (1998), Time resolved N2 triplet state vibrational populations and emissions associated with red sprites, *J. Atmos. Sol. Terr. Phys.*, *60*, 811–829, doi:10.1016/S1364-6826(98)00031-5.

Moudry, D. (2003), The dynamics and morphology of sprites, PhD thesis, Univ. of Alaska, Fairbanks.

Moudry, D., H. Stenbaek-Nielsen, D. Sentman, and E. Wescott (2003), Imaging of elves, halos and sprite initiation at 1 ms time resolution, *J. Atmos. Sol. Terr. Phys.*, *65*, 509–518, doi:10.1016/S1364-6826(02)00323-1.

Neubert, T. (2003), On sprites and their exotic kin, *Science*, *300*, 747–749, doi:10.1126/science.1083006.

Pancheshnyi, S., M. Nudnova, and A. Starikovskii (2005), Development of a cathode-directed streamer discharge in air at different pressures: Experiment and comparison with direct numerical simulation, *Phys. Rev. E*, *71*(1), 016407, doi:10.1103/PhysRevE.71.016407.

Pancheshnyi, S., B. Eismann, G. J. M. Hagelaar, and L. C. Pitchford (2008), Zdplaskin: Zero-dimensional plasma kinetics. [Available at http://www.zdplaskin.laplace.univ-tlse.fr/.]

Parra-Rojas, F. C., A. Luque, and F. J. Gordillo-Vázquez (2013a), Chemical and electrical impact of lightning on the Earth mesosphere: The case of sprite halos, *J. Geophys. Res. Space Physics*, *118*, 5190–5214, doi:10.1002/jgra.50449.

Parra-Rojas, F. C., M. Passas, E. Carrasco, A. Luque, I. Tanarro, M. Simek, and F. J. Gordillo-Vázquez (2013b), Spectroscopic diagnostics of laboratory air plasmas as a benchmark for spectral rotational (gas) temperature determination in TLEs, *J. Geophys. Res. Space Physics*, *118*, 4649–4661, doi:10.1002/jgra.50433.

Pasko, V. P. (2003), Atmospheric physics: Electric jets, *Nature*, *423*, 927–929.

Pasko, V. P., and H. C. Stenbaek-Nielsen (2002), Diffuse and streamer regions of sprites, *Geophys. Res. Lett.*, *29*(10), 1440, doi:10.1029/2001GL014241.

Pasko, V. P., U. S. Inan, Y. N. Taranenko, and T. F. Bell (1995), Heating, ionization and upward discharges in the mesosphere due to intense quasi-electrostatic thundercloud fields, *Geophys. Res. Lett.*, *22*, 365–368, doi:10.1029/95GL00008.

Pasko, V. P., U. S. Inan, T. F. Bell, and Y. N. Taranenko (1997), Sprites produced by quasi-electrostatic heating and ionization in the lower ionosphere, *J. Geophys. Res.*, *102*, 4529–4561, doi:10.1029/96JA03528.

Pasko, V. P., U. S. Inan, and T. F. Bell (1998), Spatial structure of sprites, *Geophys. Res. Lett.*, *25*, 2123–2126, doi:10.1029/98GL01242.

Passas, M., J. Sánchez, A. Luque, and F. J. Gordillo-Vázquez (2014), Transient upper atmospheric plasmas: Sprites and halos, *IEEE Trans. Plasma Sci.*, *42*, 2664–2665, doi:10.1109/TPS.2014.2329320.

Picard, R. H., U. S. Inan, V. P. Pasko, J. R. Winick, and P. P. Wintersteiner (1997), Infrared glow above thunderstorms?, *Geophys. Res. Lett.*, *24*, 2635–2638, doi:10.1029/97GL02753.

Rairden, R. L., and S. B. Mende (1995), Time resolved sprite imagery, *Geophys. Res. Lett.*, *22*, 3465–3468, doi:10.1029/95GL03332.

Raizer, Y. P. (1991), *Gas Discharge Physics*, Springer, Berlin, Germany.

Raizer, Y. P., G. M. Milikh, M. N. Shneider, and S. V. Novakovski (1998), Long streamers in the upper atmosphere above thundercloud, *J. Phys. D*, *31*, 3255, doi:10.1088/0022-3727/31/22/014.

Rodger, C. J., A. Seppälä, and M. A. Clilverd (2008), Significance of transient luminous events to neutral chemistry: Experimental measurements, *Geophys. Res. Lett.*, *35*, L07803, doi:10.1029/2008GL033221.

Sentman, D. D., and H. C. Stenbaek-Nielsen (2009), Chemical effects of weak electric fields in the trailing columns of sprite streamers, *Plasma Sources Sci. Technol.*, *18*(3), 034012, doi:10.1088/0963-0252/18/3/034012.

Sentman, D. D., and E. M. Wescott (1995), Red sprites and blue jets: Thunderstorm-excited optical emissions in the stratosphere, mesosphere, and ionosphere, *Phys. Plasmas*, *2*, 2514–2522, doi:10.1063/1.871213.

Sentman, D. D., E. M. Wescott, D. L. Osborne, D. L. Hampton, and M. J. Heavner (1995), Preliminary results from the Sprites94 aircraft campaign: 1. Red sprites, *Geophys. Res. Lett.*, *22*, 1205–1208, doi:10.1029/95GL00583.

Sentman, D. D., H. C. Stenbaek-Nielsen, M. G. McHarg, and J. S. Morrill (2008), Plasma chemistry of sprite streamers, *J. Geophys. Res.*, *113*, D11112, doi:10.1029/2007JD008941.

Shao, X. M., E. H. Lay, and A. R. Jacobson (2012), Reduction of electron density in the night-time lower ionosphere in response to a thunderstorm, *Nat. Geosci.*, *6*, 29–33, doi:10.1038/NGEO1668.

Stanley, M., P. Krehbiel, M. Brook, C. Moore, W. Rison, and B. Abrahams (1999), High speed video of initial sprite development, *Geophys. Res. Lett.*, *26*, 3201–3204, doi:10.1029/1999GL010673.

Stanley, M., M. Brook, P. Krehbiel, and S. A. Cummer (2000), Detection of daytime sprites via a unique sprite ELF signature, *Geophys. Res. Lett.*, *27*, 871–874, doi:10.1029/1999GL010769.
Stenbaek-Nielsen, H. C., and M. G. McHarg (2008), High time-resolution sprite imaging: Observations and implications, *J. Phys. D*, *41*(23), 234009, doi:10.1088/0022-3727/41/23/234009.
Stenbaek-Nielsen, H. C., D. R. Moudry, E. M. Wescott, D. D. Sentman, and F. T. Sao Sabbas (2000), Sprites and possible mesospheric effects, *Geophys. Res. Lett.*, *27*, 3829–3832, doi:10.1029/2000GL003827.
Stenbaek-Nielsen, H. C., M. G. McHarg, T. Kanmae, and D. D. Sentman (2007), Observed emission rates in sprite streamer heads, *Geophys. Res. Lett.*, *34*, L11105, doi:10.1029/2007GL029881.
Stenbaek-Nielsen, H. C., T. Kanmae, M. G. McHarg, and R. Haaland (2013), High-speed observations of sprite streamers, *Surv. Geophys.*, *34*, 769–795, doi:10.1007/s10712-013-9224-4.
Taranenko, Y. N., U. S. Inan, and T. F. Bell (1993), The interaction with the lower ionosphere of electromagnetic pulses from lightning: Heating, attachment and ionization, *Geophys. Res. Lett.*, *20*(23), 1539–1542.
Taylor, M. J., et al. (2008), Rare measurements of a sprite with halo event driven by a negative lightning discharge over Argentina, *Geophys. Res. Lett.*, *35*, L14812, doi:10.1029/2008GL033984.
Vaughan, O. H., R. Blakeslee, W. L. Boeck, B. Vonnegut, M. Brook, and J. McKune (1992), A cloud-to-space lightning as recorded by the space shuttle payload-bay TV cameras, *Mon. Weather Rev.*, *120*, 1459–1461, doi:10.1175/1520-0493(1992)120<1459:ACTSLA>2.0.CO;2.
Wilson, C. T. R. (1925), The electric field of a thundercloud and some of its effects, *Proc. Phys. Soc. London*, *37*, 32D.
Winckler, J. R., W. A. Lyons, T. E. Nelson, and R. J. Nemzek (1996), New high-resolution ground-based studies of sprites, *J. Geophys. Res.*, *101*, 6997–7004, doi:10.1029/95JD03443.
Winkler, H., and J. Nothold (2014), The chemistry of daytime sprite streamers—A model study, *Atmos. Chem. Phys.*, *14*, 3545–3556, doi:10.5194/acp-14-3545-2014.
Yair, Y., et al. (2004), New observations of sprites from the space shuttle, *J. Geophys. Res.*, *109*, D15201, doi:10.1029/2003JD004497.
Yelinov, P. I. Y., A. Mishev, and L. Mateev (2009), Model for induced ionization by galactic cosmic rays in the Earth atmosphere and ionosphere, *Adv. Space Res.*, *44*, 1002–1007, doi:10.1016/j.asr.2009.06.006.